Dark Spot Detection from SAR Intensity Imagery with Spatial Density Thresholding for Oil Spill Monitoring

by

Yuanming Shu

A thesis
presented to the University of Waterloo
in fulfillment of the
thesis requirement for the degree of
Master of Science
in
Geography

Waterloo, Ontario, Canada, 2010

Author's Declaration

I hereby declare that I am the sole author of this thesis. This is a true copy of the thesis, including any required final revisions, as accepted by my examiners.

I understand that my thesis may be made electronically available to the public.

Abstract

Since the 1980s, satellite-borne synthetic aperture radar (SAR) has been investigated for early warning and monitoring of marine oil spills to permit effective satellite surveillance in the marine environment.

Automated detection of oil spills from satellite SAR intensity imagery consists of three steps: 1) Detection of dark spots; 2) Extraction of features from the detected dark spots; and 3) Classification of the dark spots into oil spills and look-alikes. However, marine oil spill detection is a very difficult and challenging task. Open questions exist in each of the three stages.

In this thesis, the focus is on the first stage—dark spot detection. An efficient and effective dark spot detection method is critical and fundamental for developing an automated oil spill detection system. A novel method for this task is presented. The key to the method is utilizing the spatial density feature to enhance the separability of dark spots and the background. After an adaptive intensity thresholding, a spatial density thresholding is further used to differentiate dark spots from the background. The proposed method was applied to a evaluation dataset with 60 RADARSAT-1 ScanSAR Narrow Beam intensity images containing oil spill anomalies. The experimental results obtained from the test dataset demonstrate that the proposed method for dark spot detection is fast, robust and effective. Recommendations are given for future research to be conducted to ensure that this procedure goes beyond the prototype stage and becomes a practical application.

Acknowledgements

Finally, and most importantly, I am deeply indebted to my parents for their love, encouragement and inspiration. Without them, I would not have been able to succeed in this M. Sc. study with one and a half years in a foreign country.

Table of Contents

List of Figures

List of Tables

Chapter 1

Introduction

In this chapter, background on oil spill pollution problem as well as its satellite surveillance using synthetic aperture radar (SAR) is given in Section 1.1. Problems and challenges in oil spill detection with SAR are described in Section 1.2. The objectives and scope of the thesis are presented in Section 1.3. The thesis structure is outlined in Section 1.4.

1.1 Background

1.1.1 Oil Spill Pollution Problem

Marine oil pollution is a major threat to the fragile marine and coastal ecosystems. Once it is spilled, toxic effects of the floating oil on the sea surface can cause significant decrease in the biomass of planktons living in the upper layers of the sea, which further affects the stability of the food chain in the marine ecosystem (Gin et al., 2001). Seabirds suffer from feather contamination as a result of direct contact with oil spills. The damaged feather will reduce their resistance to temperature fluctuations, impair their buoyancy in water, and result in loss of flight ability. The ingestion of oil spills can cause damages to birds' organs, which leads to loss of eggs or even direct death (Tseng, 1999). The livelihood of people along the coastal areas may be also threatened by marine oil pollution, particularly those who rely on fishing and tourism for living. (Jha et al, 2008).

1

The main sources of marine oil pollution are discharges coming from ships or offshore platforms, which can be accidental or deliberate (Topouzelis, 2008). On August 4, 2006, oil leaking from M/V Westwood Anette at Squamish dock terminal, just north of Vancouver, British Columbia, Canada, costs $1 million to cleanup. The most expensive oil spill in history is Exxon Valdez occurred in Prince William Sound, Alaska, on March 24, 1989. The vessel spilled 10.8 million gallons crude oil that eventually covered 11,000 square miles of the sea. The cleanup cost alone runs up to US$2.5 billion (NOAA 1992). Ship routine operations also release oil ballast water into the sea (Ferraro et al., 2007). Compared to the oil leakage resulted by the ship accidents, these "deliberate" oil discharges are found to be a much greater threat to marine and coastal ecosystem (Pavalakis et al., 1996; European Space Agency, 1998).

1.1.2 Satellite Sensors for Oil Spill Surveillance

Efficient monitoring and early warning are essential for preventing the widespread damage of oil pollution and mitigating its adverse impact to ecosystems. The different means for oil spill monitoring includes vessel, airplane, and satellite surveillance. The vessel covers a very limited area, but remains necessary in case that oil sampling is required. The combined use of satellite and aircraft surveillance is a cost-effective way for the purpose. Satellite monitoring helps identify parties that potentially respond to oil pollution in a large area, while aircraft patrolling helps verify oil spills and catch polluters. Various sensors can be utilized to perform the task, including the ultraviolet sensors, visible sensors, infrared sensors, and microwave sensors. The most up-to-date comparison of different sensors for oil spill detection can be found in Jia et al. (2008).

2

During the past two decades, much attention has been given to the utilization of SAR. SAR is an active microwave imaging system that transmits short directional electromagnetic (EM) wave pulses and then operates as a sensitive receiver to record the backscatter signals to form a two-dimensional (2-D) image. SAR is an appropriate tool for oil spill monitoring due to the following reasons:

1) As an active microwave system which can provide the energy on its own, SAR is independent of solar illumination and can work day and night (Richards & Jia, 2006). Empirically, illegal oil discharges often occur at night (Gade & Alpers, 1999).

2) The short directional EM wave can penetrate clouds, fog, and rain, which enables SAR to work independently of weather conditions (Richards & Jia, 2006). Most of oil tanker accidents are associated with bad weather (Hofer, 2003).

3) The satellite SAR image can monitor large ocean area, the cost of which is much lower than that of air patrolling (Brekke & Solberg, 2005).

4) Due to the dampening effect of oil spills, they are differentiable from the surrounding spill-free sea on the SAR imagery and can be detected by the SAR sensor (Alpers & Huhnerfuss, 1989).

A SAR sensor can be described by the frequency band, polarization, incidence angle, swath width, and spatial resolution. Usually, for oil spill detection, large swath widths are chosen at the expense of lower resolution because it is in our interest to cover a large area even if very small oil spills cannot be detected. The commonly used SAR sensors for oil spill monitoring from literature include RADARSAT-1, ENVISAT, ERS-2 (Brekke & Solberg, 2005; Topouzelis, 2008). Table 1.1 presents satellite SAR sensors that have been commonly used for oil spill

monitoring. Canadian Space Agency's RADARSAT program is to strategically improve Canada's marine monitoring capability. RADARSAT-2 and the future RADARSAT Constellation will ensure continuity with RADARSAT-1, but offer new modes of operation with enhanced capabilities. The newly launched Italian Cosmo-Skymed and German TerraSAR-X also pose better potential for oil spill monitoring, with their multimode data acquisitions, capability of higher spatial resolution, and shorter revisit time.

Table 1.1. List of SAR imaging satellites that have been commonly used for oil spill monitoring (adapted from Brekke & Solberg, 2005).

SAR sensor	Band/Mode*	Nominal resolution (m)	Pixel spacing (m)	Swath width (km)	Incidence angle (°)	Polarization
ERS-2	C/PRI	30×26.3	12.5×12.5	100	20-26	VV
ENVISAT	C/IM	30×30	12.5×12.5	100	15-45	VV & HH
ENVISAT	C/WSM	150×150	75×75	400	16-44	VV & HH
RADARSAT-1	C/SSN	50×50	25×25	300	20-46	HH
RADARSAT-1	C/SSW	100×100	50×50	500	20-49	HH

*PRI-Precision Image Mode, IM-Image Mode, SSN-ScanSAR Narrow, SSW-ScanSAR Wide, WSM-Wide Swath Mode.

1.1.3 Automated Detection of Oil Spills from SAR Intensity Imagery

The detectability of oil spills by SAR sensors lies on the fact that oil spills dampen the short waves and reduce the backscattered energy from the sea surface resulting in dark regions on SAR intensity imagery (Alpers & Huhnerfuss, 1989). However, other man-made or natural phenomena may also dampen the sea surface and create dark regions on SAR imagery, similar to the representation of oil spills, for example, the wake of a moving ship, low wind areas, organic films and eddies (Alpers et al., 1991; Hovland et al., 1994). They are termed as look-alikes in oil spill detection (Brekke, & Solberg, 2005). Also, the visibility of oil spills on SAR imagery is affected by the wind level on the sea surface. Only in a certain range of wind speeds, approximately from 2-3 m/sec to 10-14 m/sec, oil spills can be detected by SAR sensors (Girard-Ardhuin et al., 2005).

The detection of oil spills from SAR imagery can be divided into three stages: 1) Detection of dark spots (suspicious oil spills); 2) Extraction of features from the detected dark spots; and 3) Classification of the dark spots (oil spills and look-alikes) (Brekke & Solberg, 2005). This can be done manually, or automatically. In the manual detection, a trained human operator has to go through the entire image, find possible oil spills, and discriminate between the oil spills and the look-alikes.

Though a trained human operator is able to detect oil spills from SAR images with some confidence, it is time consuming. It is also labour-intensive given a large number of SAR images

5

to be analyzed annually for oil spill monitoring. Besides, manual detection is constrained by the knowledge and experience of the human operator, whose results are subjective. A trend to develop fast, reliable, and automated oil spill detection systems, has therefore arisen recently (Nirchio et al., 2005; Karathanassi et al., 2006; Keramitsoglou et al., 2006; Solberg et al., 2007; Topouzelis et al., 2007).

1.2 Problem Addressed

As a preliminary task of oil spill detection, dark spot detection is critical and fundamental prior to feature extraction and classification. Therefore, unless an oil spill could be detected at this first stage, it would never be detected at a later stage. Also, the accuracies of feature extraction and classification greatly rely on the dark spot detection. Some high level features such as geometric feature and context feature (Brekke & Solberg, 2005) are sensitive to the result of dark spot detection. Inappropriate detection in the first step will cause the deviation in the extraction of such features, which further leads to the misclassification in the final stage. Besides, dark spot detection is traditionally the most-time consuming among the three stages. The entire SAR image has to be searched to identify locations of dark spots. In contrast, feature extraction and classification only need to work on detected dark spots. Once the dark spots have been detected, the feature extraction and classification need only a few seconds to complete their actions. Therefore, an efficient and effective dark spot detection method is essential for developing an automated oil spill detection system.

However, two main difficulties lie in the detection of dark spots: 1) SAR imagery is highly speckled due to the constructive and destructive interferences of the reflections from sea surface (Richards & Jia, 2006). Intensity value may show considerably variability even in the neighbourhood of a uniform region. 2) Contrasts between dark areas and the surroundings are varying, which depends on local sea state, oil spill type, and resolution and incidence angle of SAR imagery (Topouzelis, 2008). Various efforts on dark spot detection have been made during the past decades. However, the above two difficulties ruled out achieving a robust as well as fast processing method for dark spot detection so far. In most cases speed is sacrificed for robustness or vice versa in a few other cases. Lack of efficient and effective dark spot detection method has become one of major obstacles to the development of automated oil spill detection system using SAR imagery (Topouzelis, 2008).

1.3 Thesis Objectives and Scope

Oil spill detection using SAR is a challenging problem. Open questions exist in each of the three stages in developing an automated oil spill detection system (Brekke & Solberg, 2005; Topouzelis, 2008). Due to limited time for data collection and experiments, this thesis tackles the challenging problem of dark spot detection using the single frequency and single polarization SAR intensity images, which have been commonly used in oil spill detection. The general goal of this thesis is to develop a fast, robust, and effective method for automated dark spot detection from SAR intensity imagery. More specifically, the objectives of this study include to

1) Study and analyse the complexity and uncertainty of dark spot detection from SAR

7

intensity imagery.

2) Design and develop a framework for dark spot detection from SAR intensity imagery that can be incorporated into an automated oil spill detection system for practical monitoring.

3) Design and implement the evaluation approach that can assess the performance of the proposed dark spot detection method.

1.4 Thesis Outlines

This thesis is organized as follows:

Chapter 2 gives an introduction to a SAR imaging system with emphasis on those related to oil spill detection. This chapter also reviews existing methods for dark spot detection methods which are relevant to this study.

Chapter 3 presents a novel method which integrates the spatial density feature with the intensity feature to tackle the difficulties existing in the automated dark spot detection.

Chapter 4 demonstrates the results of dark spot detection by the proposed method on different SAR intensity images. The automatically detected results are qualitatively and quantitatively evaluated with respect to manual detection. A comparison with the classic level set method is given.

Chapter 5 summaries the findings of this thesis and also suggests avenues for future research.

Chapter 2

Related Work on Dark Spot Detection

SAR with capability of all weather and day/night imaging acquisition is especially useful for oil spill monitoring. With the progress of SAR technology, ample data is now available for monitoring of marine oil spill pollution. However, the capability of detecting oil spills from SAR imagery is limited due to lack of fast, reliable, accurate and automated detection systems.

In this chapter, the satellite SAR imaging principle is first briefly introduced in Section 2.1. The detectability of oil spills from SAR intensity imagery is described in Section 2.2. Existing oil spill detection systems and approaches which are relevant to dark spot detection are reviewed in Section 2.3-2.5. A summary of this chapter is given in the last section.

2.1 SAR Imaging Principle

SAR is an active microwave system that transmits a sequence of microwave pulses and then operators as a receiver to record the returned signals from the ground surface (Richards & Jia, 2006). The SAR imagery is formed by the backscattered signals. The intensities of the signals are controlled by the interaction between the microwave energy and the surface, which is a function of several variables. These variables include prosperities of the SAR system (frequency, polarization, viewing geometry, etc.) and properties of the surface (surface roughness, geometric

shapes, moisture content, etc.). One of major consequences of such imaging mechanism is the

presence of speckle noises in SAR images. Unlike system noises, speckle noises are not real

noises but electromagnetic measurements, which follow the coherent principle (Oliver &

Ouegan, 1998). The classical SAR imaging model assumes that the presences of a large number

of discrete point scatters are within each resolution cell of a distributed ground target (see Figure

2.1).
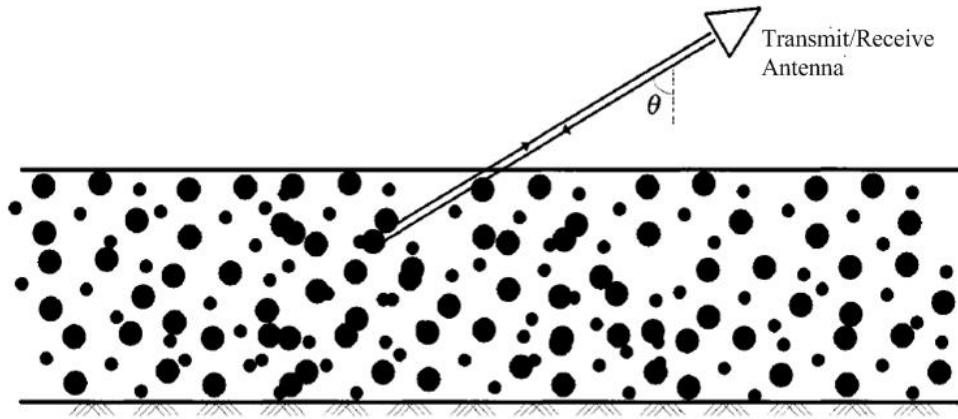
Figure 2.1. Representation of a distributed ground target contaning a large number of discrete point scatters (Oliver & Quegan, 1998).

When illuminated by the SAR beam, every scatter contributes a backscattering wave with phase

and amplitude changing. The total returned incidence microwave is a vector summation of each

individual microwave backscattered at each position (Oliver & Quegan, 1998),

$$Ae^{j\phi} = \sum_{i=1}^{N} A_i e^{j\phi_i} = \sum_{i=1}^{N} A_i (\cos\phi_i + \sin\phi_i) \tag{2.1}$$

where A_i is the scattering amplitude and ϕ_i is the scattering phase at position i. N is the total number of scatters within the resolution cell. For a uniform distributed ground target, characteristics of individual scatters are similar. The amplitude of individual scatter A_i can be assumed to be identical at different positions of the resolution cell. However, as the slant range resolution of the SAR beam is typically many wavelengths across, the phase of individual scatter ϕ_i at different position of the resolution cell will become very different, which can be thought of as being uniform in $[\pi, -\pi]$ and independent of the amplitude A_i (Oliver & Quegan, 1998). Therefore, great random fluctuations in backscattered microwave signals can be observed as "salt-and-pepper" speckles even in a uniform region of SAR imagery (see Figure 2.2).

2.2 Detectability of Oil Spills in SAR Intensity Imagery

2.2.1 SAR Imaging of the Sea

Sea has a large dielectric constant. The microwave signals cannot penetrate the surface of the sea beyond a few millimeters. Hence the sea scattering process is dominated by surface scattering, where surface roughness significantly influences microwave energy backscattered from the sea
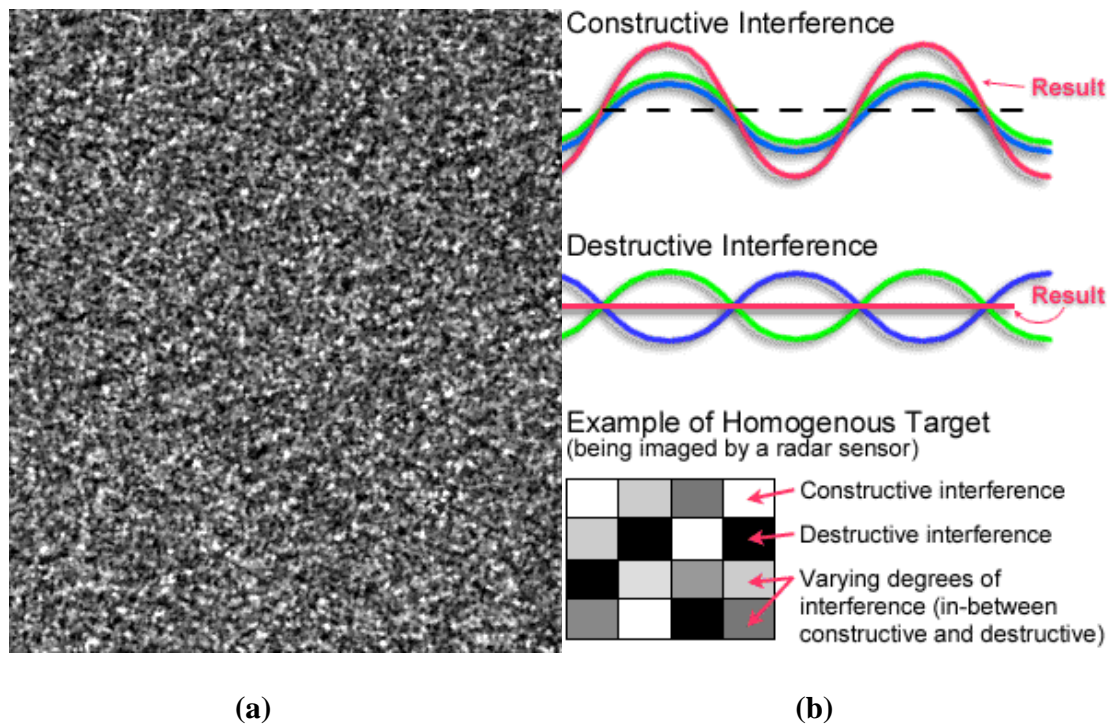
Figure 2.2. Illustration of speckle noises (adapted from Canada Centre for Remote Sensing, 2009): (a) Speckle noises in a homogeneous region, (b) Principle of speckle noises

surface (Martin, 2004; Gens, 2008). The sea surface roughness is dependent on the sea waves which are controlled by the wind. In general, the incidence microwave energy is scattered from short waves (less than 1m in wavelength) and reflected from long waves (100 m in wavelength) (Ulaby et al., 1982). The backscattered energy increases as the increase of wind speed. For the satellite SAR sensors whose incidence angles are usually between 20°-70°, there is no microwave energy reflected back from long waves. The sea backscatter is governed by the scattering from the short waves riding on surface of the long waves, either very short gravity waves or capillary waves. These waves are called "Bragg waves", which can cause "Bragg

backscatter" from the ocean surface. According to Ulaby et al. (1982), the backscatter exhibits strong resonances when

$$\lambda_w = \lambda / 2 \sin \theta \qquad\qquad (2.2)$$

where λ_w is the wavelength of the sea surface wave; λ is the radar wavelength; θ is the local incidence angle. Other than the surface roughness described above, the intensity of returned energy is also affected by the radar incidence angle. The backscatter from the sea surface decreases rapidly as the radar incidence angle increases (Clement-Colon & Yan, 2000).

As can be concluded from the description above, the SAR imaging of the sea is actually a radar backscatter mapping of ocean surface roughness. Ocean phenomena can be detected from SAR imagery only if it changes the surface roughness. Phenomena such as, oil spills, wake of moving ships, wind and rainfall can all modulate the surface roughness directly or indirectly and therefore can be observed from SAR imagery (Gens, 2008).

2.2.2 SAR Imaging of Oil Spills

The detectability of oil spills in satellite SAR intensity imagery is due to the dampening effect of oil spills on Bragg waves which results in dark regions in SAR intensity imagery. Theoretical and experimental work has been carried out to understand the dampening effect of oil spills (Alpers & Huehnerfuss, 1988; 1989). For very thin floating oil film, its elastic property gives rise

14

to local surface tension gradients, which generates longitudinal waves. When longitudinal waves and Bragg waves come in resonance, the Bragg waves experience maximum dampening. For thick oil spills, their high viscosity dampens the Bragg waves.

The potential to detect oil spills in SAR intensity images is largely affected by the wind speed. When the speed is too low, the wind has not enough power to generate sufficient sea clutter to contrast to the dampening effect of oil spills, which makes them invisible from SAR imagery. In contrast, when the speed is too high, the Bragg waves can receive enough energy to counterbalance the dampening effect of oil spills, which also makes them invisible from SAR imagery (Topouzelis et al., 2008). The minimum wind speed for oil spills to be detected from SAR imagery is in fact different from different sensors, depending on the specific radar wavelength and the incidence angle. For the satellite SAR sensors using the C-band, effective radar detection of oil spills requires wind speed from 2-3 m/sec to 10-14 m/sec (Girard-Ardhuin et al., 2005).

The wavelength and polarization of SAR sensors also affect the detectability of oil spills. Several researchers reported that the oil-water backscatter contrast decreases as the radar wavelength increases (Neville et al., 1984; Wismann et al., 1998; Gade et al, 1998). Though some studies show that there is no real difference between horizontal (HH) and vertical (VV) polarization for oil spill detection (Wismann et al., 1998), there is agreement in the literature that VV polarized images provide a better oil-water contrast than either HH or HV polarized images for the C-band (Neville et al., 1984; Singh, 1987; Masuko, 1995; Wismann et al., 1998). Even though this thesis

15

focuses on single polarization SAR images, it is worth mentioning the potential of the enhanced oil spill detectability with multi-frequency and multi-polarization SAR images (Gade et al., 1996; Maio et al., 2001; Fortuny-Guasch, 2003; Migliaccio et al., 2007).

Several man-made and natural ocean phenomena can also dampen the Bragg waves and generate dark spots in the SAR imagery, similar to the representation of oil spills. For example, turbulence generated in the water by the wake of a moving ship can produce a dark spot on the SAR image that sometimes looks quite similar to oil released from a ship. Dark regions can also result from low-wind areas, organic films, fronts, areas sheltered by land, rain cells, currents shear zones, grease ice, internal waves, upwelling zones, downwelling zones and eddies (Alpers et al., 1991; Hovland et al., 1994). These phenomena are referred as "look-alikes" in oil spill detection. To discriminate between oil spills and "look-alikes" is one of major challenges for oil spill detection.

(a)	**(b)**
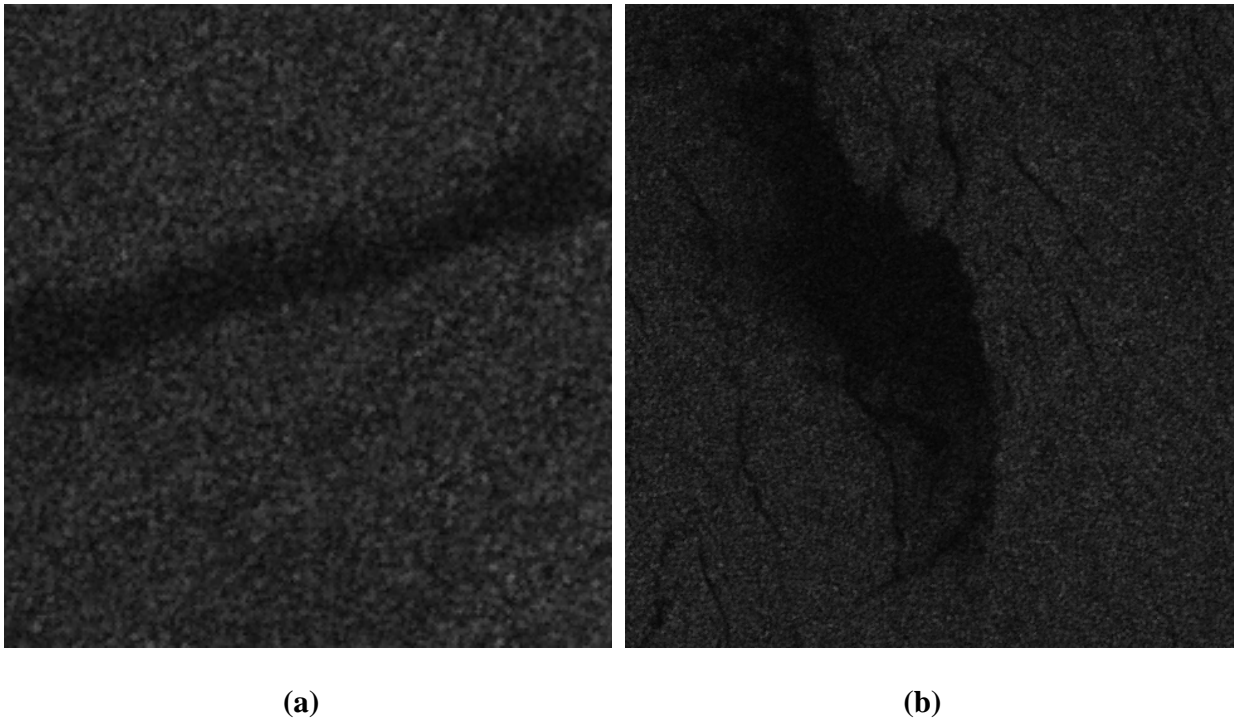
Figure 2.3. Two subscenes (256×256 pixels in dimension) of RADARSAT-1 ScanSAR Narrow Beam image covering East Coast of Canada (July 10, 2007): (a) Oil spill verified by CIS, (b) Look-alike probably caused by low wind.

detection using SAR intensity imagery. Figure 2.3 gives an example of an oil spill and a look-alike imaged by RADARSAT-1. Figure 2.3(a) shows an oil spill that was verified by Canadian Ice Service (CIS) through air patrolling. Figure 2.3(b) shows some other phenomena causing low backscattering (probably low wind area).

2.2.3 SAR Sensors for Oil Spill Detection

Evans et al. (2005) summarized all satellite SAR sensors launched in history, from Seasat (1978) to RADARSAT -2 (2007). Table 2.1 list key characteristics of the existing satellite-borne SAR

sensors. The use of SAR for oil spill monitoring can be traced back to Elachi (1980), who explored the capability of Seasat for oil spill detection. The second generation of satellite SAR sensors were launched in the 1990s, with single polarization (either horizontal or vertical), moderate spatial resolution, and wide swath coverage. The capabilities of oil spill detection with the second generation SAR sensors, such as ENVISAT, ERS-2, and RADARSAT-1, were studied in various researches (Henschel et al., 1997; Solberg & Volden, 1997; Solberg et al., 1999; Espedal & Wahl 1999; Espedal & Johannessen, 2000; Fiscella et al., 2000; Frate et al., 2000). The third generation of satellite SAR sensor was launched in the past three years, represented by Canadian RADARSAT-2, Italian Cosmo-Skymed and German TerraSAR-X. They provide better potential for oil spill detection with their multi-polarization options, higher spatial resolution and shorter revisit time (Fortuny-Guasch, 2003; Gambardella et al, 2007; Malinovsky et al., 2007; Migliaccio et al., 2007).

Table 2.1. Summary of exsiting SAR imaging satellites (extended from Evans et al., 2005)

Satellite	Country	Operative	Band	Polarization	Frequency (GHz)	Swath width (km)	Best spatial resolution(m)
Seasat	USA	1978-1978	L	HH	1.28	100	25
SIR-A	USA	1981-1981	L	HH	1.28	50	40
SIR-B	USA	1984-1984	L	HH	1.28	30	25
ERS-1	Europe	1991-2000	C	VV	5.3	100	30
JERS-1	Japan	1992-1998	L	HH	1.27	75	18
SIR-C/ XSAR	USA German/ Italy	1994-1994	C, L, X	HH, VV, HV, VH	1.28, 5.3, 9.6	10-200	30
ERS-2	Europe	1995-operating	C	VV	5.3	100	30

RADAR SAT -1	Canada	1995- operating	C	HH	5.3	100-170	10
SRTM	USA Geman	2000-2000	C, X	HH, VV	5.3	50-225	30
ENVISA T	Europe	2002- operating	C	VV, HH, VV/VH, HV/HH, VH/VV	5.33	100	30
ALOS PALSAR	Japan	2007- operating	L	VV , HH, HH/HV, VV/VH	1.27	70	10
TerraSA R-X	German	2007- operating	X	various	9.6	50	1
RADAR SAT -2	Canada	2007- operating	C	various	5.4	10-500	3
Cosmo/ Skymed Constella tion	Italy	2007 - operating	X	HH, VV, HV, VH, Dual-pol	9.6	10-200	1

2.3 Oil Spill Detection using SAR

The detection of oil spills from SAR intensity imagery can be done manually, semi-automatically or fully automatically (Topouzelis, 2008). In the manual approach, human operators are trained to analyze images for detecting oil spills. For example, Canadian Ice Service (CIS) has been designing a program ISTOP (Integrated Satellite Tracking of Pollution) since 2006 as part of its ice surveillance operational program towards effective use of RADARSAT-1 data as an aid in oil

spill detection (Gauthier et al. 2007). In ISTOP, The human image analysts first overlay several GIS files with the SAR image, including the coastline, the 200nm exclusive economic zone (EEZ), and information about the marine oil platforms. They then discriminate between possible oil spills (anomalies) and look-alikes using their experience and prior information concerning the location, the proximity to land, the weather information, the difference in shapes, and the contrast with the surrounding sea between anomalies and look-alikes. The anomalies are classified into three categories according to whether there are ships within a certain distance of the anomalies. If the anomaly is associated with a ship, it is classified as Category 1A; if there are ships within 50 km of the anomaly, it is classified as Category 1B; if no ship is within 50 km of the anomaly, it is labelled as Category 2; the anomalies that analysts have least confidence will be labeled as Category 3. The purpose of this kind of categorization is to facilitate later prosecution. Reported anomalies are immediately sent to the Canadian Coast Guard, which arranges aircraft verifications. Once an anomaly is validated as an oil spill, ships nearby will be investigated to find the source of pollution. Manual interpretation method is based on the knowledge and experience of the image analysts, thus it is time consuming, labour intensive, and subjective. Different image analysts may have different interpretation results. Such a manual interpretation method is greatly limited especially when it is applied to interpret more than 5,000 scenes annually at CIS and each takes 15-45 minutes to analyze. With the launch of RADARSAT-2 and the start-up of RADARSAT Constellation plan, more and more SAR data will be available for oil spill monitoring. The labour intensity for oil spill monitoring at CIS would expect to significantly increase. It is therefore necessary to develop an automated oil spill detection system.

Efforts related to the development of semi-automated or fully automated oil spill detection system using SAR intensity imagery have been made by several organizations. Examples include the semi-automated systems such as Ocean Monitoring Workstation (OMW) at CIS (Henschel et al. 1997), Alaska SAR Demonstration (AKDEMO) system at U. S. National Oceanic and Atmospheric Administration (NOAA) (Pichel & Clemente-Colon 2000), and a fully-automated system such as Kongsberg Satellite Services (KSAT)'s oil spill detection system at Norway (Solberg et al., 2007). The automated methods can be summarized in three stages (Brekke & Solberg, 2005): 1) Detecting all the dark spots in the image; 2) Extracting features from detected dark spots, such as intensity feature, geometric feature, and context feature; and 3) Classifying dark spots into oil spills or look-alikes. The semi-automated method usually covers the first step- dark spot detection, and the feature extraction and classification are done by human image analysts. Figure 2.4 illustrates the flowchart of the automated oil spill detection.

```
         ┌─────────────────────────┐
         │     Input SAR Image     │
         └─────────────────────────┘
                      │
                      ▼
         ┌─────────────────────────┐
         │   Dark Spot Detection   │
         └─────────────────────────┘
                      │
                      ▼
         ┌─────────────────────────┐
         │    Feature Extraction   │
         └─────────────────────────┘
                      │
                      ▼
         ┌─────────────────────────┐
         │      Classification     │
         └─────────────────────────┘
                      │
                      ▼
         ┌─────────────────────────┐
         │   Detected Oil Spills   │
         └─────────────────────────┘
```
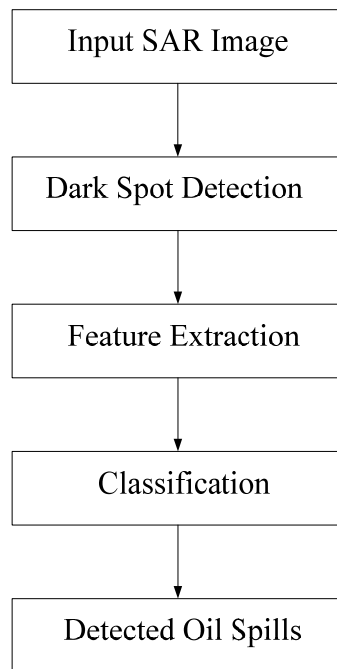
Figure 2.4. Flowchart of an automated oil spill detection method (adapted from Brekke & Solberg, 2005).

Three main difficulties exist for automated methods: 1) SAR imagery is highly speckled. Intensity value may show considerably variability even in the neighborhood of a uniform region (Richards & Jia, 2006); 2) Contrasts between dark spots and the background are varying, under different local sea state, oil spill type, resolution, and incidence angle of SAR imagery (Topouzelis, 2008). For example, fresh oil spills have weaker dampening effect on Bragg waves and thus appears to be brighter than older oil spills (Topouzelis, 2008); and 3) Look-alikes also create dark spots in the SAR imagery, which needs to be differentiated from dark spots generated by oil spills (Topouzelis, 2008). However, oil spills are extreme events. Studies on oil spill classification are often constrained by lack of sufficient training data. Due to the above difficulties, automated methods are not very popular for current operational oil spill detection.

22

For example, the CIS's experience indicates that the OMW is limited to dark spot detection and the output from OMW is not operationally used due to the large number of false targets. As a result, CIS currently detects oil spills primarily through manual interpretation of SAR images.

As the first and primary stage of oil spill detection, dark spot detection is critical and fundamental for oil spill detection. The accuracy of feature extraction and classification greatly depends on the result of dark spot detection. Also, dark spot detection is traditionally most-time consuming among the three stages. The entire SAR image has to be searched to identify locations of dark spots. In contrast, feature extraction and classification only need to work on detected dark spots. Therefore, a fast, reliable and effective dark spot detection method is essential for developing an automated oil spill detection system. Several efforts have been made to achieve the objective during the past few years. For the purpose of discussion, they are grouped into four classes and reviewed in details in separate sections. They include classification-based method, segmentation-based method, multi-scale analysis, and other methods.

2.4 Dark Spot Detection Methods

2.4.1 Classification-based Method

Dark spot detection can be treated as a classification problem, classifying pixels into "dark spots" and "background". Artificial neural network is a mathematical model that simulates the

structure and mechanism of human brain for classification (Bishop, 2006). Topouzelis et al. (2008) examined the capability of two types of feed-forward neural network, Multilayer Perceptron (MLP) and the Radial Basis Function (RBF) networks, for detect dark detection from high-resolution SAR imagery. They found that MLP networks achieved the most reliable results for dark spot detection in all the examined cases.

Rather than treat the dark spot detection as a classification problem, it can be also considered as an abnormal detection problem, finding the dark spots that are abnormal to the background. Mercier & Girard-Ardhuin (2006) proposed a semi-supervised dark spot detection method based on the idea. SAR image is first decomposed into multi-scale layers by using the wavelet transformation. Information including both radiometric and texture features is then extracted from multi-scale layers. A specific kernel is developed to perform abnormal detection by utilizing the information extracted. In their experiment, their method takes a minute on a 1.8-GHz Linux Laptop to classify a 512×512 SAR image and the results are effective.

However, the classification-based method needs to involve human supervision in the training procedure. Since dark spots may have various contrasts towards surroundings under different conditions, training process has to be carried out every time for different SAR images. As a result, the classification-based method is often limited in application to an automated oil spill detection system.

2.4.2 Segmentation-based method

In computer vision, segmentation refers to the process of partitioning a digital image into multiple segments that share certain visual characteristics (Shapiro & Stockman, 2001). The dark spot detection from SAR imagery is in fact a segmentation problem, aiming to partition a SAR image into dark spots and the background. Several methods based on various segmentation techniques have been proposed for dark spot detection, including thresholding, region growing, level set segmentation, and so on (Huang et al., 2005; Karanthanassi, 2006; Solberg, 2007).

Thresholding

Thresholding is the simplest image segmentation method. During the thresholding process, a threshold value is first set according to certain rules. Pixels are then partitioned into "objects" and "background" according to the threshold. For example, pixels are labelled as "objects" if their value is greater than the threshold and as "background" otherwise. One of major advantages of thresholding method is its simplicity in computation, which can achieve a high speed in segmentation process. As a result, it is widely adopted in dark spot detection, where computational efficiency is crucial. Several approaches based on various thresholding techniques have been proposed.

Fiscella et al. (2000) used a global threshold for the entire SAR image. It is set as one half of the average Normalized Radars Cross-Section (NRCS) of the SAR image. Pixels with NRCS below

the threshold in the image are regarded as dark spots. The detected dark spots with area too small are removed, since small spills are not significant from the costal guard point of view. The detected spots with area too large are also rejected, since the large ones are probably no wind areas. Similar to Fiscella's method, Nirchio et al. (2005) used the NRSC minus the standard deviation as the global threshold.

Solberg et al. (2007) detected dark spots using an adaptive thresholding method. A detecting window is moving through the whole image. The threshold is calculated locally, within the area of a moving window, which is set for dark spots as ΔdB_k below the mean value in a moving window. The value of ΔdB_k is calculated by the ratio of the standard deviation to the mean value in the local window. The thresholding is combined with a multi-scale approach and a clustering step to effectively separate dark spots from background.

Chang et al. (2008) built a framework for detected dark spots from SAR intensity images based on moment preserving method and region-merging techniques. In their method, the SAR image is first split by utilizing a moment preserving thresholding, which aims to find a threshold that make the moment of image invariant during the segmentation. A region-merging techniques based on N-nearest-neighbour rule is then used to remove the small isolated regions and get more integrated segmentation.

Though the thresholding method can achieve fast detecting speed, it may also lead to a large number of false alarms in the process due to the effect of speckle noises. Post-processing, such as

the clustering step in Solberg et al. (2007), or region-merging in Chang et al. (2008), is usually necessary to eliminate these detected false alarms. However, no sufficient data has been demonstrated in their studies to verify the robustness of these post-processing techniques for dark spot detection in various conditions. For example, Chang et al. (2008) only showed their detection results in four simple scenes. And Solberg et al. (2007) reported their algorithm achieved bad detection results in two complex scenes.

Region Growing

Region growing is another popular method that is widely used for image segmentation. In region growing process, a set of pixels are first selected as "initial points". The method then examines the neighbouring pixels of the initial "seed points" and determines whether the pixel should be added to the seed point or not (Gonzalez & Woods, 2002).

The segmentation module in the well-known object-oriented classification software "eCognition" is based on the region growing method (Definiens, 2000). Karathanassi et al. (2006) developed a method for dark spot detection in the eCognition environment. A combination of 3×3 Lee filter and 7×7 Local Region filter was first implemented to reduce the speckle noises. A bottom-up region-growing technique starting with one-pixel objects is used for the segmentation. Pixels with similar spectral properties are merged together. A "merging cost" is assigned to each merging. The process stops when the cost exceeds the predefined threshold. The problem with this method is how to set the merging and stopping criteria. Past experiences with

27

eCognition indicate that there are usually many parameters that need to be tuned back and forth in order to achieve effective results. The method is not suitable for developing an automated oil spill detection system.

Level Set Segmentation

Level set method is a numerical technique for propagating interfaces, which is widely used in various disciplines, such as image processing, computational graphics, computer geometry, optimization and computational fluid dynamics (Osher & Fedkiw, 2002). In terms of image segmentation, the key idea behind the level set method is to represent the 2D curve as the zero level set of a 3D surface and evolve the surface by solving the partial differential equation (PDE) until the curve arrives on the true boundaries of objects in the image. Compared to the explicit representation by parameterizing the boundary of the curve in the well-known "snakes" segmentation model (Kass et al., 1987), the use of implicit function brings great benefits for curve evolution. It avoids the problems with instabilities, deformation of curve element and complicated surgery for topological repair of the curve existing in traditional explicit representation method. Therefore, it would be much easier to work with the level set function for curve evolution than with the curve directly. Interested readers are referred to (Osher & Fedkiw 2002) for the detail explanation.

Huang et al. (2005) detected dark spots by using a partial differential equation (PDE)-based level set method. Starting from an initial curve generated by threshold segmentation, the level set

function is propagated under the control of the speed function which is determined by both the image intensity gradient and the curvature flow. As the propagation of level set function, the zero level set will move to the true boundaries of dark spots.

Karantzalos & Argialas (2008) also applied level set segmentation method to dark spot detection. In their method, a combination of anisotropic diffusion filtering and morphological levelling filtering is first used to reduce speckle noises to some degree. The Chan-Vese level set segmentation model is then applied to segment an image into dark spots and background.

Though level set is proved to be an excellent model for image segmentation, it is time-consuming. Whilst the implicit representation of 2D contours into a 3D surface brings lots of benefits for curve evolution, it also introduces large computation burden. For a image with size of $m \times n$, complexity $O(n \times m)$ is required at each iteration of curve evolution (Adalstenisson, & Sethian, 1995). Also, the nature of the level set segmentation is a two-phase classification model, which fails to consider the situation that a SAR image may not contain any oil spills. In that case, the two-phase assumption will fail and methods based on the model work improperly.

2.4.3 Multi-Scale Analysis

Multi-scale analysis is a useful tool for image processing. The basic idea of multi-scale analysis is to build an image pyramid by decomposing original image into multi-resolution layers and

analyze the image at different scales. The analysis results obtained on separate scales are then combined to form the final results (Gonzalez & Woods, 2002).

Chen et al. (1997) developed a dark spot detection method by using the linear Gaussian transformation, which consists of two stages. In the first stage, a multi-resolution layer is generated by sequentially reducing the original image with a unit of 2×2 pixels. In the second stage, the Difference of Gaussian and the Laplace of Gaussian is applied to each layer and a top-down approach is used to integrate the detections in the different layers.

Liu et al. (1997) used wavelet analysis of SAR images for coastal watch. The original image is first decomposed into multiple layers by 2D Mexican hat wavelet transformation. The detection of dark spots created by oil spills is carried out in a small scale layer (e.g., 2 units of pixel spacing). Edge detection and edge linking algorithms are implemented on the layer to extract the boundaries of dark spots.

Derrode & Mercier (2007) developed a vector hidden Markov chain (HMC) model adapted to a multi-scale representation of the SAR image using wavelet. The original image is first decomposed into multiple layers by wavelet transformation. The observation from each layer is considered as a component of a vector data. A vector based classification is implemented based on the HMC model, which yields an unsupervised segmentation method for dark spot detection.

The multi-scale analysis is demonstrated to be a powerful tool to handle the speckle noises as well as the difficulties caused by various contrasts of dark spots towards background. However, the major challenge for multi-scale methods is how to effectively and efficiently combine the analysis at different scales. Chen et al. (1997) used the top-down approach to address the problem, while Liu et al. (1997) just simple analyze the image at a small scale. Whether these techniques are robust to automated dark spot detection under various conditions was not demonstrated in their experiments. Derrode & Mercier (2007) developed a more sophisticated model for the task, which characterizes the observations at multiple scales as a vector data and implements vector-classification algorithm based on the HMC model. However, whether the observations from the different scales should be treated equally in the vector data as Derrode & Mercier did is not clear. No enough data were available to validate the robustness of their method, either. Moreover, the implementation of HMC model is time consuming and is not suited to dealing with a large SAR image. Lastly, Derrode & Mercier's unsupervised segmentation method is in fact a two-phase unsupervised classification method. It fails to consider the situation when a SAR image of the sea surface contains no oil spill.

2.4.4 Other Methods

Maio et al. (2001) proposed a method for dark spot detection from polarimetric SAR images based on the Constant False Alarm Rate (CFAR) detection, an adaptive algorithm widely used to detect target returns against a background in SAR imagery (Novak et al., 1993). In Maio's method, the probability density function of ocean background is first estimated from the image, which is assumed as Gaussian distribution. A threshold is set in order to achieve a required

31

probability of false alarm (also known as CFAR). Pixels with value below the threshold are assumed as dark spots and as background otherwise. The method can also be applied to single polarized SAR intensity imagery. The CFAR detection method can achieve high speed in detection. However, as indicated, dark spots have various contrasts towards the background. When the distribution of dark spots and background is close to each other, the CFAR would detect a number of false alarms.

Li & Li (2010) developed a new method for automated detection of dark spots from SAR intensity imagery, which combines a marked point process, the Bayesian inference and the Markov chain Monte Carlo (MCMC) technique. In this method, a marked point process defined by density function with respect to Poisson measure is used to characterize the locations of oil spills and statistical distribution of intensities for the corresponding pixels in the SAR data. The reversible jump Markov chain Monte Carlo (RJMCMC) algorithm is used to simulate the process from the density function. The optimal locations of oil spills are found by maximizing the density function. Li & Li's method is robust to speckle noises and achieved promising results in their experiment. However, the nature of the method is still a two-phase classification method. It has the common problem that any two-phase classification method will have on dark spot detection (see Section 3.1). Also, the RJMCMC simulation is time-consuming. As reported in Li & Li's experiment, detection in a single SAR image with a dimension of 512×512 pixels spend 20 minutes under the MATLAB 7.0 platform.

2.5 Chapter Summary

In this chapter, topics concerning satellite SAR imaging system and detectability of oil spills in SAR intensity imagery have been reviewed. Understanding these is the precondition for designing effective dark spot detection method from SAR intensity imagery. A review of existing dark spot detection methods has been presented. As seen from the review, most of previous methods detect dark spots by utilizing the intensity feature. However, the effect of speckle noises and various contrasts between dark spots and the background bring great difficulties to the detection in the intensity domain. To overcome the problem, multi-scale approaches decompose image into multi-resolution layers and implement the detections at different scales. However, how to identify the proper detection scales and how to combine the detections on different scales are unsolved issues. Up to now, none of existing methods is able to detect dark spots effectively and efficiently. In most cases, speed is sacrificed for robustness or vice versa in a few other cases. In the next chapter, the attention is driven from the intensity domain to the spatial domain. A novel spatial density thresholding method is proposed for automated dark spot detection from SAR intensity imagery.

Chapter 3

Dark Spot Detection by Spatial Density Thresholding

To detect dark spots effectively and efficiently, a new method called spatial density thresholding is proposed in this chapter. Apart from utilizing the common intensity feature of dark spots, this method employs the spatial density feature to enhance the separability between dark spots and the background.

In this chapter, general principle of the proposed methodology is first explained in Section 3.1. The proposed method is detailed from Section 3.2 to 3.5. A summary of this chapter is given in the last section.

3.1 Principle of Proposed Method

The proposed method is motivated by the nature of the pixels' spatial distribution as observed in Figure 3.1. Different marks represent pixels with different intensities. The triangles represent the pixels with low intensity values and the circles are the pixels with high intensity values. If the triangles are uniformly distributed in the spatial domain (see Figure 3.1(a)), the observed region would be thought as a homogeneous background (e.g., sea). And these triangles are evident as speckle noises. However, in Figure 3.2(b), triangles exhibit two types of spatial distributions: locations insides the dashed box with high density of triangles and locations outside the dashed

box with low density of triangles. In such a case, the triangles inside the dashed box would be thought as some dark spot (e.g., an oil spill), while the rest of them are speckle noises. The validity of the above interpretation is guaranteed by the fundamental property of SAR imagery described in Section 2.1. That is, the constructive and destructive interferences of the reflection from surfaces have random spatial variations. Therefore, if the triangles in Figure 3.1(b) are all speckles, they should be uniformly distributed in the region like the one in Figure 3.1(a), rather than exhibit such a clustering in the dashed box. In the same way, these triangles in Figure 3.1(b) are unlikely to be all dark spot pixels. Otherwise, they should not exhibit two types of spatial distributions. Triangles inside the dashed box where the density is high are most likely to be the real dark spot, while the other ones are probably the speckle noises in the background.

Let's further explain how the above observation can help with developing an effective dark spot detection method. Suppose the Bayes criterion for detecting a dark spot states that (Oliver & Quegan, 1998)

$$P(T \mid x) = P(x \mid T)P(T) / P(x) \tag{3.1}$$
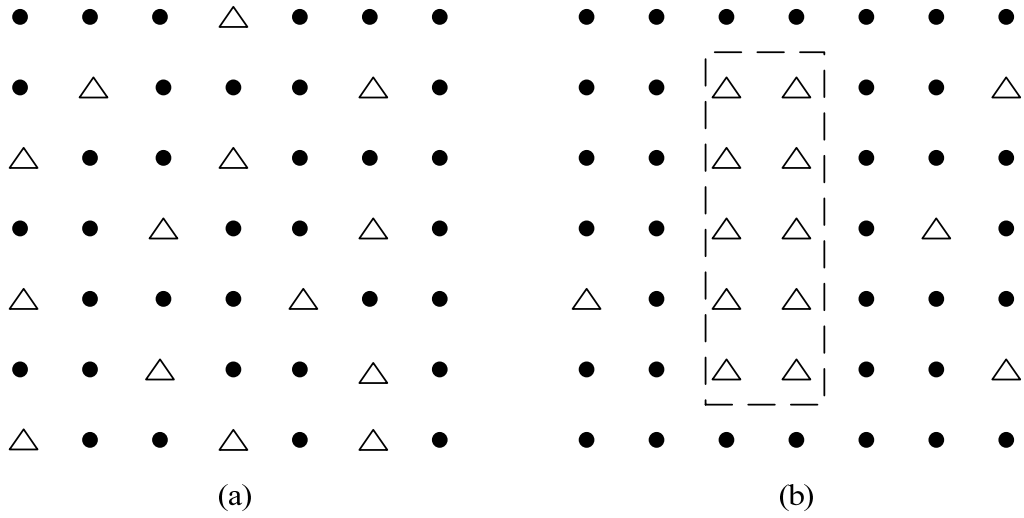
Figure 3.1. Illustration of a homogeneous area (a) and a heterogeneous area (b).

.

where x is the intensity; $P(T \mid x)$ is the posterior probability of a dark spot given the intensity; $P(x \mid T)$ is the likelihood probability of intensity x given a dark spot is present; $P(T)$ is the priori probability. Similarly for the background,

$$P(B \mid x) = P(x \mid B)P(B) / P(x) \tag{3.2}$$

The Maximum-a-Posteriori (MAP) criterion implies that a dark spot should be considered present when

$$\frac{P(T \mid x)}{P(B \mid x)} > 1 \tag{3.3}$$

36

from which

$$\frac{P(x|T)}{P(x|B)} > \frac{P(B)}{P(T)} \qquad (3.4)$$

If the background and the dark spot are assumed to be equally likely, equation (3.4) reduces to

$$\frac{P(x|T)}{P(x|B)} > 1 \qquad (3.5)$$

If the distribution of the background and the dark spot are further assumed to be Gaussian distribution with equal variance, the optimal threshold (in terms of MAP criterion) for separating a dark spot from the background in this condition is the average mean value of both Gaussian distributions T_1, as illustrated in Figure 3.2 (Fukunaga, 1990). The probability of a false alarm in the background region would be the area marked by real line, which is given by

$$P_{fa} = \int_0^t P(x|B)dx \qquad (3.6)$$

And the corresponding detection probability of a dark spot is the area marked by the dashed line, which is given by

$$P_d = \int_0^t P(x \mid T) dx \qquad\qquad (3.7)$$

When equation (3.3) the likelihood probability functions of a dark spot and background are separate from each other, the dark spot can be detected from the background with few false alarms by just using an appropriate intensity threshold. However, dark spots may have various contrasts towards the background under different conditions. When their likelihood probability functions become close to each other, even the optimal threshold T_I would still result in a large number of false alarms.
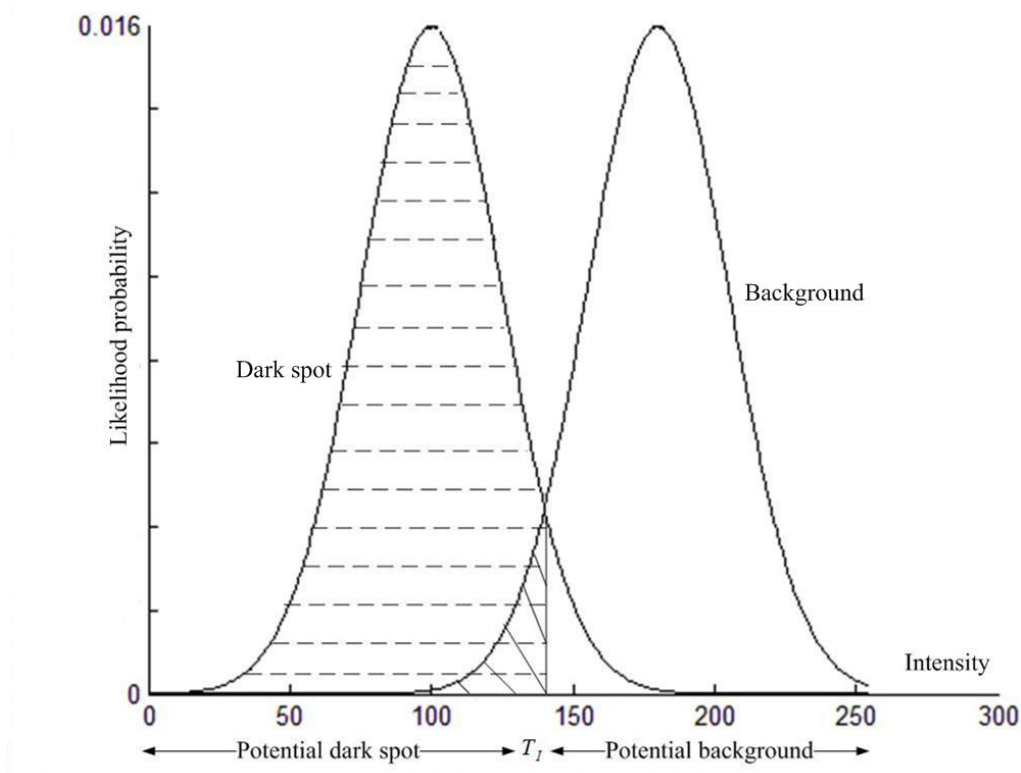

Figure 3.2. Illustration of likelihood probability of a dark spot and background.

However, if the spatial distribution of intensity is considered, the dark spot and the background can be separated further. Before addressing the idea in detail, it needs to clarify some terminologies to avoid confusion. In this thesis, pixels with intensity below the intensity threshold T_I are referred as "potential dark spot pixels" or "dark pixels" interchangeably. Pixels with intensities above T_I are referred as "potential background pixels" or "light pixels" throughout the context.

From equations (3.5), (3.6) and (3.7), it is not hard to see that the probability of occurrence of a dark pixel in a dark spot is higher than the one in background. Also, according to the principles of SAR imaging described in Section 2.1, intensities are uniformly distributed in a uniform region. It therefore can be concluded the spatial density of dark pixels is higher in the dark spot than the one in the background. If the density of dark pixels is to be estimated, the false alarms can be further separated from the real dark spot by using the following Criterion 1:

"The dark pixels with density above certain threshold T_D are the real dark spot pixels while the other ones below are the background pixels."

Similarly, the density of light pixels is expected to be lower in the dark spot than the one in the background. Therefore, if the density of light pixels is to be estimated, the real dark spot pixels that were incorrectly regarded as the potential background pixels can be further separate from the background by using the following Criterion 2:

"The light pixels with density below certain threshold $T_D^{'}$ are the real dark spot pixels while the other ones above are the background pixels."

As a result, the detection probability of a dark spot increases, while the probability of a false alarm decreases. It may be further noticed that the space domain is fully occupied by potential dark spot and background pixels. Locations with high density of dark pixels would definitely have low density of light pixels. Therefore only one criterion is needed to have the dark spot and the background further separated. That is,

"Locations with the density of dark (light) pixels above (below) certain threshold T_D ($T_D^{'}$) are the real dark spot pixels while the others are the background pixels."

So far, we have known that the spatial density feature can help further discriminate between the dark spot and the background from the deduction described above. However, what if all the assumptions made in the above deduction fail in practice? For example, the distributions of the background and the dark spot are not Gaussian distribution with the same variance. Or, the background and the dark spot are not equally likely to appear in the SAR image. Can the spatial density feature still work in those cases? In fact, due to the dampening effect of oil spills, it can be always directly assumed that the probability of occurrence of a dark (light) pixel is higher (lower) in the dark spot than in the background without making any assumptions about the likelihood probabilities and prior probabilities of the dark spot and the background. Here the dark pixels refereed to pixels with intensities below a threshold set by certain rule, such as the

```
┌─────────────────────────┐
│    Detecting Window     │
└─────────────────────────┘
             │
             ▼
┌─────────────────────────┐      ┌ ─ ─ ─ ─ ─ ─ ─ ─ ─ ─ ─ ─ ┐
│      Pre-processing     │◀─ ─ ─   Image Enhancement
└─────────────────────────┘         Gaussian Filtering
             │                    └ ─ ─ ─ ─ ─ ─ ─ ─ ─ ─ ─ ─ ┘
             ▼
┌─────────────────────────┐      ┌ ─ ─ ─ ─ ─ ─ ─ ─ ─ ─ ─ ─ ┐
│   Intensity Thresholding│◀─ ─ ─   Otsu's Adaptive Thresholding
└─────────────────────────┘       └ ─ ─ ─ ─ ─ ─ ─ ─ ─ ─ ─ ─ ┘
             │
             ▼
┌─────────────────────────┐      ┌ ─ ─ ─ ─ ─ ─ ─ ─ ─ ─ ─ ─ ┐
│ Spatial Density Threshoding│◀─ ─ Density Estimation
└─────────────────────────┘         Density Normalization
             │                      Density Thresholding
             ▼                    └ ─ ─ ─ ─ ─ ─ ─ ─ ─ ─ ─ ─ ┘
┌─────────────────────────┐      ┌ ─ ─ ─ ─ ─ ─ ─ ─ ─ ─ ─ ─ ┐
│     Post-processing     │◀─ ─ ─   Area Thresholding
└─────────────────────────┘         Contrast Thresholding
             │                      Boundary Extraction
             ▼                    └ ─ ─ ─ ─ ─ ─ ─ ─ ─ ─ ─ ─ ┘
┌─────────────────────────┐
│   Detected Dark Spots   │
└─────────────────────────┘
```
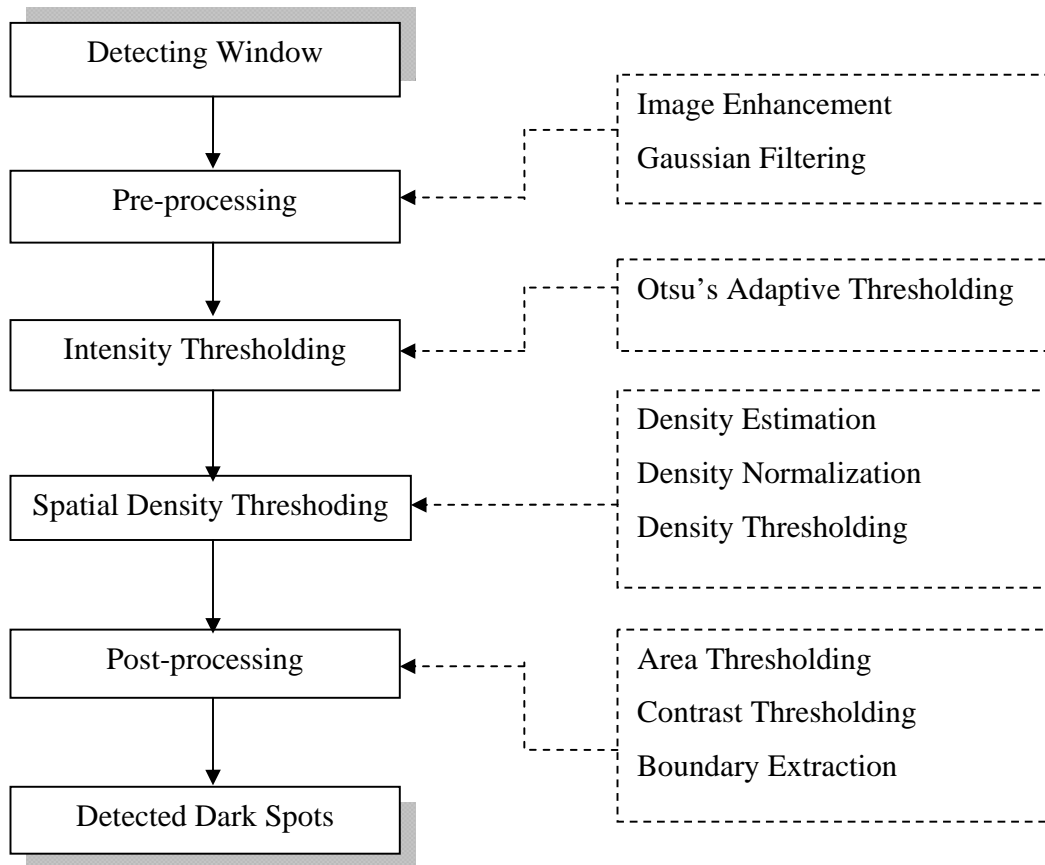
Figure 3.3. Flowchart of main procedures of the proposed method.

MAP or the Otsu's criterion described in Section 3.3. And the light pixels are the ones with intensities above the threshold. Also, the second condition that intensities are uniformly distributed in a uniform region is always guaranteed by the principle of SAR imaging described in Section 2.1. Therefore, it still can be concluded that the spatial density of dark (light) pixels is higher (lower) in the dark spot than the one in the background. Hence the spatial density feature can still be used to help further discriminate between the dark spot and the background, even

though those assumptions about probabilities are not satisfied in practical SAR images used for the oil spill detection.

Based on the idea on spatial density thresholding described above, a new method for dark spot detection is proposed. In this method, a detecting window is passed through the SAR image. First, an adaptive intensity thresholding is implemented to each window. Pixels with intensity below the intensity threshold is regarded as potential dark spot pixels and the others are potential background pixels. Second, the density of potential background pixels is estimated using kernel density estimation. A spatial density threshold is selected and pixels with density below the threshold are regarded as the real dark spot pixels while the others are the background pixels. Third, an area and a contrast threshold are further used to eliminate false alarms left. Holes inside dark spots are considered as dark spots. Boundaries of dark spots are extracted. Lastly, the individual detection results are mosaicked to form the final result. A flowchart of the main procedures in the proposed method is illustrated in Figure 3.3 and their details are presented from Section 3.2 to 3.5.

3.2 Pre-processing

A $N \times N$ Gaussian filter with the standard deviation of σ is used to smooth the original image, whose impulse response $g(x, y)$ is given by (Gonzalez & Woods, 2002),

$$g(x, y) = \frac{1}{\sqrt{2\pi}\sigma} e^{-\frac{x^2 + y^2}{2\sigma^2}} \tag{3.8}$$

where x and y are the distance from the origin in the horizontal and vertical axis respectively.
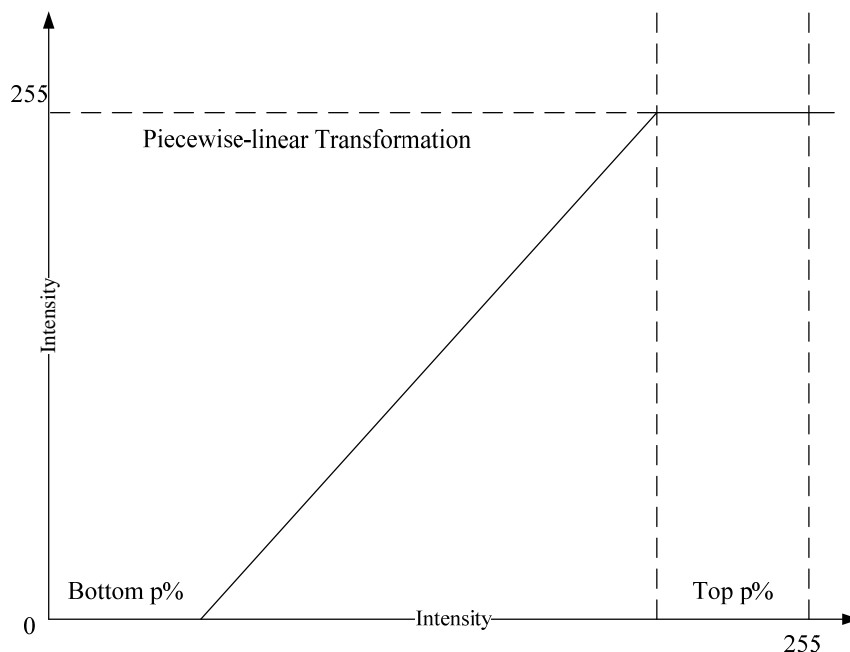

Figure 3.4. Illustration of the piecewise-linear transformation.

The histogram of the original image is then adjusted by a piecewise-linear transformation. The bottom p_1 percentages of all pixel values are specified as 0, while the top p_2 percentages are specified as 255. The rest of pixel values are stretched to the range from 0 to 255 by a linear transformation. Figure 3.4 illustrates the piecewise-linear transformation. The use of Gaussian filter and piecewise-linear transformation can reduce the degree of speckle noises and enhance the contrast between dark spots and background. On one hand, it improves the visual quality of SAR image which benefits the visual evaluation of detection results (see Section 4.3). On the

other hand, it proves more stable intensity threshold in intensity segmentation (see Section 3.3) and stable contrast threshold in post-processing (see Section 3.4).

3.3 Intensity Thresholding

Since no prior knowledge is available on the distributions of the dark spot and the background, it is intractable to find the optimal threshold in terms of the MAP criterion. The thresholding algorithm proposed by Otsu (1979) is used to find a threshold that approximates the optimal threshold by MAP criterion. Suppose the intensity of given image can be represented in L gray levels. The probability distribution of pixels at level i is defined by,

$$p_i = \frac{n_i}{N}, \quad p_i > 0, \sum_{i=1}^{L} p_i = 1 \tag{3.9}$$

where n_i is number of pixels at level i and N is the total number of pixels in the given image. Suppose we want to find a threshold at level k to group pixels of the given SAR image into two classes, dark spot and background. Let C_s denotes dark spot pixels with levels from 1 to k, and C_l denotes background pixels with level from $k+1$ to L. The class means are given by,

$$\mu_s = \sum_{i=1}^{k} i \Pr(i \mid C_s) \tag{3.10}$$

$$\mu_l = \sum_{i=k+1}^{L} i \Pr(i \mid C_l) \tag{3.11}$$

where

$$\Pr(i \mid C_s) = \frac{p_i}{\sum_{i=1}^{k} p_i} \tag{3.12}$$

$$\Pr(i \mid C_l) = \frac{p_i}{\sum_{i=k+1}^{L} p_i} \tag{3.13}$$

The class variances are given by,

$$\sigma_s^2 = \sum_{i=1}^{k} (i - \mu_s)^2 \Pr(i \mid C_s) \tag{3.14}$$

$$\sigma_l^2 = \sum_{i=k+1}^{L} (i - \mu_l)^2 \Pr(i \mid C_l) \tag{3.15}$$

The between-class variance and within-class variance are given by,

$$\sigma_W^2 = \omega_s \sigma_s^2 + \omega_l \sigma_l^2 \tag{3.16}$$

$$\sigma_B^2 = \omega_s \omega_l (\mu_s - \mu_l)^2 \tag{3.17}$$

where

$$\omega_s = \sum_{i=1}^{k} p_i, \qquad \omega_l = \sum_{i=k+1}^{L} p_i \qquad\qquad (3.18)$$

According to Otsu's method, the optimal threshold k is that one that maximizes the ratio of the between-class variance to the within-class variance, which is given by

$$\lambda = \frac{\sigma_B^2}{\sigma_W^2} \qquad\qquad (3.19)$$

After the threshold is calculated, pixels with intensity above the threshold are regarded as the potential background pixels and the others are the potential dark spot pixels.

3.4 Spatial Density Thresholding

The density of potential background pixels within the detecting window is estimated using kernel density estimation. The kernel density estimation, also known as the Parzen window technique in pattern recognition literature (Fukunaga, 1990) is the most popular density estimation method. Given n sample data points $x_i, i = 1,..., n$ on $\boldsymbol{R}$ drawn from probability density $f(x)$, its kernel density estimator computed in the point x is given by

$$\breve{g}(x) = \frac{1}{nt} \sum_{i=1}^{n} K(\frac{x - x_i}{t}) \tag{3.20}$$

where $K(x)$ is the kernel function and t is the bandwidth. $K(x)$ is required to satisfy the following two conditions:

$$\int_{R} K(x) du = 1 \quad and \quad K(x) \geq 0 \tag{3.21}$$

The most widely used kernel is the Gaussian of zero mean and unit variance which is given by

$$\breve{g}(x;t) = \frac{1}{n\sqrt{2\pi t^2}} \sum_{i=1}^{n} e^{-(x-x_i)^2 / 2t^2} \tag{3.22}$$

The only unknown parameter in equation (3.22) is the bandwidth t. The optimal choice of t is important, since the performance of $\breve{g}$ as an estimator of f depends on its value. The most widely used criterion of performance of estimator in equation (3.23) is the Mean Integrated Squared Error (MISE) (Jones et al., 1996):

$$MISE\{\breve{g}\}(t) = E_f \int [\breve{g}(x;t) - f(x)]^2 dx = \int (E_f[\breve{g}(x;t)] - f(x))^2 dx + \int Var_f[\breve{g}(x;t)]dx \tag{3.23}$$

The first component of equation (3.23) is referred as point-wise bias and the second component is referred as integrated point-wise variance (Jones et al., 1996). Interested readers are referred to the survey of Jones et al. (1996) for the details of bandwidth selection techniques.

Botev (2009) proposed a novel method for finding the optimal bandwidth t in terms of MISE criterion, which is used in the thesis. In Botev (2009), finding the optimal bandwidth of Gaussian kernel density estimator in terms of MISE criterion is equivalent to finding the optimal mixing time, say $\breve{t}^*$, of the diffusion process governed by,

$$\frac{\partial}{\partial t}\breve{g}(x;t) = \frac{1}{2}\frac{\partial^2}{\partial x^2}\breve{g}(x;t), \quad x \in R, t > 0, \tag{3.24}$$

with initial condition $\breve{g}(x;0) = \Delta(x) =$ empirical density. For more mathematical details on the diffusion process, its solution, and its connection to statistical smoothing, readers are referred to Lindeberg (1994) and Chaudhuri & Marron (2000).

To find a universal density threshold for all conditions, the estimated density is normalized by,

$$\breve{g}(x;t)_{norm} = \frac{\breve{g}(x;t) - \min(\breve{g}(x;t))}{\max(\breve{g}(x;t)) - \min(\breve{g}(x;t))} \tag{3.25}$$

where $\breve{g}(x;t)_{norm}$ is the normalized density, $\min(\breve{g}(x;t))$ is the minimum value of $\breve{g}(x;t)$ and $\max(\breve{g}(x;t))$ is the maximum of $\breve{g}(x;t)$. The normalized density is then transformed to the 8-bit ranging from 0 to 255. The selection of a density threshold is based on the idea that, if a dark spot exists then it must have density abnormal to the background. Therefore, after the transformation, the densities of real dark spot pixels are expected to be concentrated in a narrow part in the beginning of 8-bit range, where the threshold can be set correspondingly. The 8-bit transformation is empirical. It was motivated by benefiting the visual threshold selection at first, since after the 8-bit transformation we can display the density map as image and select the threshold visually. The experiment shows the threshold works well after such transformation. After the density threshold is selected, pixels with density below the threshold are regarded as the real dark spot and the one above are the real background.

The density of potential dark spot pixels instead of potential background pixels can also be estimated for density threshold segmentation. However, the former is found to less reliable for density threshold selection than the latter from the extensive experiments.

3.5 Post-processing

During the detection process, some regions may have been incorrectly detected as dark spots as a result of the incidental errors. An area threshold T_A and a contrast threshold T_c are used to eliminate these false targets. The average contrast between a detected region and background is given by

$$C_i = \frac{u_B - u_i}{\sigma_B} \tag{3.26}$$

where u_i is the average intensity of the detected region i; u_B is the average intensity of background and σ_B is the intensity variance of the background. Only regions with area above T_A and with average contrast above T_c are regarded as real dark spots. Holes inside the dark spot which are generated as a result of errors will be filled by using morphological dilation (Soille, 1999). After the dark spot regions are extracted, an edge detection algorithm is used to extract the boundaries of the detected dark spots (Li et al., 2008). Following the definition of 8-neighbourhoods shown in Figure 3.5, the boundary pixel of the dark spots is determined if it is a contour pixel and satisfies the condition, $0 < N(p) < 8$. $N(p)$ is the number of nonzero neighbours of pixel p which is given by

$$N(p) = \sum_{i=0}^{7} p_i \tag{3.27}$$

P_0	P_1	P_2
P_7	P	P_3
P_6	P_5	P_4

Figure 3.5. Neighborhood arrangement (Li et al., 2008).

3.6 Chapter Summary

In this chapter, a new dark spot detection method has been proposed. The key to the proposed method is to decompose the detection process into two stages: 1) Detection with the common intensity feature, and 2) Detection with the innovative spatial density feature. The introducing of spatial density feature can further discriminate between dark spots and background. Its motivation and theoretical reasoning have been described. The details of implementation of the proposed method have been presented.

Chapter 4

Results and Evaluation

In this chapter, the developed method is applied to a test dataset collected from the oil-spill target database of the ISTOP program to evaluate its performance. The properties of the test dataset are described in Section 4.1. The evaluation methods are presented in Section 4.2. The experimental results are analyzed in Section 4.3. A summary of this chapter is given in the last section.

4.1 Evaluation Dataset

In order to evaluate the effectiveness and efficiency of the proposed method, this study utilized an evaluation dataset collected from the oil-spill target database of the ISTOP program at CIS, Environment Canada in Ottawa. At CIS, a human analyst visually interprets potential dark spots to be oil spills (called anomalies) in RADARSAT-1 ScanSAR Narrow Beam images. Reported anomalies are immediately sent to the Canadian Coast Guard, which arranges aircraft verifications. In the meantime, reported anomalies are stored into the oil-spill target database. In this study, sub-images within the vicinity of the areas that contain anomalies are clipped from entire SAR images to evaluate the performance of the proposed method. The evaluation dataset are RADARSAT-1 ScanSAR Narrow Beam intensity images, C-band with HH polarization and 50 m in spatial resolution. The evaluation dataset contains a total of 30 images with a dimension of $256{\times}256$ pixels, 20 images with a dimension of $512{\times}512$ pixels, 8 images with a dimension

of 1024×1024 pixels, 1 image with a dimension of 2048×2048 pixels and 1 image with a dimension of 4096×4096 pixels. It covers all available anomaly cases detected under different conditions between 2006 and 2008.

4.2 Evaluation Methods

The program for the proposed method was developed and evaluated on the PC-based MATLAB 7.0 platform. The processor of the PC is an Intel Pentium dual-core with a speed of 2.00 GHz and the RAM memory is 2.00 GB. The proposed method is tuned and applied to all the evaluation images using the same parameters. Table 4.1 give the parameter value used in this experiment where N is the size of the Gaussian filter (see Section 3.2), σ is the standard deviation of Gaussian filter (see Section 3.2), p_1 is the top percentages of the piecewise linear histogram transformation (see Section 3.2), p_2 is the bottom percentages of the piecewise linear histogram transformation (see Section 3.2), T_D is the spatial density threshold (see Section 3.4), T_A is the area threshold (see Section 3.5); and T_c is the contrast threshold (see Section 3.5). The parameters for Gaussian filter and linear histogram transformation are just set by using default setting in the MATLAB functions contained in its image processing toolbox. The area threshold T_A is set as 100, because small oil spills are not significant in the sense of marine oil pollution monitoring. The spatial density threshold T_D and contrast threshold T_c are tuned back and forth during the experiment to make detection on all the 60 evaluation images acceptable by visual inspection. The detecting window is selected to have a size of 256×256 pixels, which is a

suitable scale particularly for oil spill detection. False targets occupying large areas, such as low-wind areas, will not be detected under such scale. The step size for the detection is 224 pixels, with an overlap of 32×256 pixels between the consecutive two detections.

Table 4.1. The parameters used in the proposed method.

N	σ	p_1	p_2	T_D	T_A	T_c
3	0.1	1%	1%	35	100	6.2

The computer-extracted dark spot boundaries are overlaid on the original image to visually evaluate the performance of the proposed method. Comparison between the proposed method and the Chan-Vese level set method (Chan & Vese, 2001) are presented on some typical evaluation images. Before the implementation of level set segmentation, the speckle reducing anisotropic diffusion (SRAD) filter (Yu & Acton, 2002) and the piecewise-linear histogram transformation (see Section 3.2.1) are used to reduce the speckle noises and enhance the image contrast. The reasons to choose the Chan-Vese level set method for comparison are: 1) It is the core technique in Karantzalos & Argialas' method, one of latest work on dark spot detection (Karantzalos & Argialas, 2008). However, Karantzalos & Argialas' program is not available for direct comparison. By comparing to the Chan-Vese level set method, the effectiveness of the proposed method in the thesis can be examined. 2) The Chan-Vese level set method is in fact an unsupervised two-phase classification method. By comparing to the method, the advantage of the proposed method over the two-phase classification methods can be investigated.

To assess the accuracy of detection results quantitatively, a reference dataset was produced by manual photo-interpretation. Due to the speckle noise and various contrasts of dark spots, manual interpretation may also become very difficult in some occasions. There's no gold standard for manual digitalization on SAR imagery. Therefore, in this thesis, the computer-extracted boundaries are used as an aid for manual digitalization. Unless there is enough reason for a human analyst to reject the result of computer-extracted boundaries according to the manual interpretation, they are followed during the digitization. The computer-extracted boundaries are compared to the reference dataset. The buffer zone approach proposed by Li et al. (2008) is used for accuracy evaluation, including commission error, omission error and average error. Figure 4.1 shows the commission error in Li's buffer zone approach. The basic idea is to create a buffer around the manually digitized line. The part out of the buffer will be accounted as the
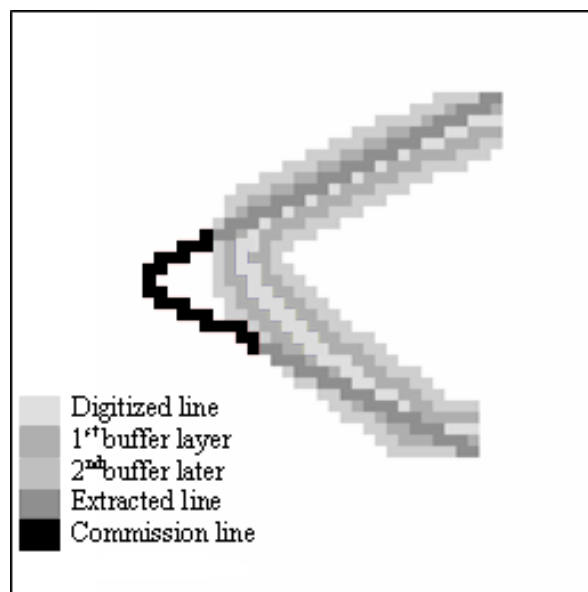

 Figure 4.1. Illustration of buffer zone structure and commission error (adapted from Li et al, 2008).

55

commission error as shown in Figure 4.1. Similarly, when the computer-extracted line and manually digitized line switch their positions in Figure 4.1, the commission error becomes the omission error.

The commission error is defined by,

$$COM = \frac{N_{EL} - N_{ELinMLB}}{N_{EL}} \tag{4.1}$$

where $N_{ELinMLB}$ is the number of pixels on the computer-extracted line within the buffer of manually digitized line and N_{EL} is the number of pixels on the computer-extracted line. The omission is defined by,

$$OM = \frac{N_{ML} - N_{MLinELB}}{N_{ML}} \tag{4.2}$$

where $N_{MLinELB}$ is the number of pixels on the manually digitized line within the buffer of computer-extracted line and N_{ML} is the number of pixels on the manually digitized line. The distribution probability of the computer-extracted line on buffer layers for the manually digitized line can be calculated as follows,

$$pd(l) = \frac{N_{ELinFLB}}{N_{ML}} \qquad\qquad (4.3)$$

where $l = 0, 1, 2, ..., n$ is the index of buffer layers; n is the total number of buffer zone. $l = 0$ is the manually digitized line, and $N_{ELinFLB}$ is the number of pixels on the computer-extracted line within l th buffer layer. The average error can be calculated by,

$$AE = \sum_{l}^{n} l * pd(l) \qquad\qquad (4.4)$$

As an additional evaluation, the average number of detected false alarms per detecting window and the average detecting speed per detecting window are also used.

4.3 Results and Discussions

Two sample evaluation images were selected to illustrate the results of the proposed method at each step. Figures 4.2(a) and (b) show the two images, one contains a dark spot while the other is homogeneous background. Figures 4.2(c) and (d) show the results after pre-processing. As seen from the figures, the contrasts of the images are enhanced after the pre-processing, which makes the dark spot detection more easily. Figures 4.2(e) and (f) show the results after adaptive intensity threshold segmentation. The black pixels are the potential background spot pixels and the white pixels are the potential dark spot pixels. As can be easily noticed in Figure 4.2(e), the density of black pixels is generally higher in the background than the one in the dark spot. Figure

4.2(g) and (h) show the results after normalized density estimation. The dark colour indicates the low density area, while the white colour indicates the high density area. Figures 4.2(i) and (j) show the results after spatial density threshold segmentation. The number of false alarms is greatly reduced afterwards. Figures 4.2(k) and (l) show the final results after eliminating the regions below the area and contrast threshold. In Figure 4.2(k), the extracted boundary of the dark spot (white line) is overlaid on the contrast enhanced image. Visual inspection shows the extracted boundary and the true dark spot boundary match quite well. In contrast, the image in Figure 4.2(l) containing no dark spot has nothing left. The situation in Figure 4.2(l) is often ignored by the two-phase classification based methods, such as level set (Karantzalos & Argialas, 2008), and marked point process (Li & Li, 2010). Figure 4.3 illustrates the detection results achieved by the level set method. The curve evolution starts from a circle initialed at the center of the image. The iteration number is set as 1500. Parameters for the level set method have been tuned for each image in order to achieve the optimal result in terms of visual inspection. The extracted boundary of the dark spot (white line) is overlaid on the contrast enhanced image. As shown in Figure 4.3(a), the level set method achieves an acceptable result when there is dark spot in the image. However, when there's no dark spot in the image, the result it obtained is very bad (see Figure 4.3(b)).

(a) Original image I
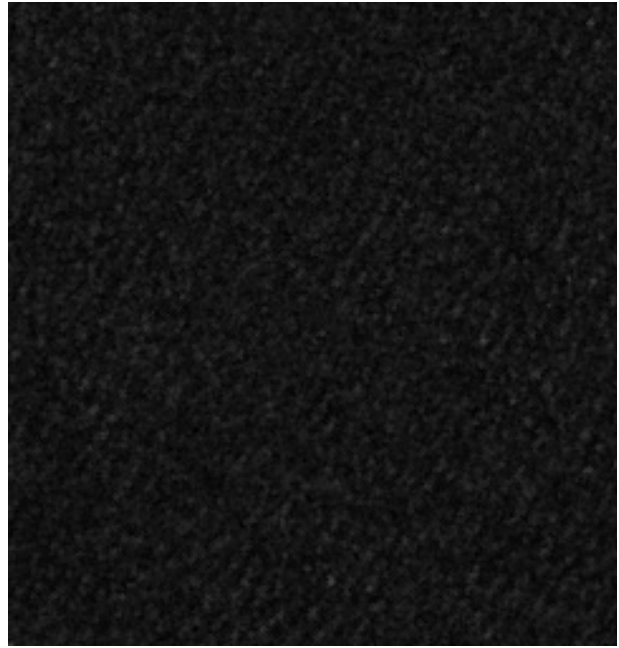
(b) Original image II

(c) Pre-processing I
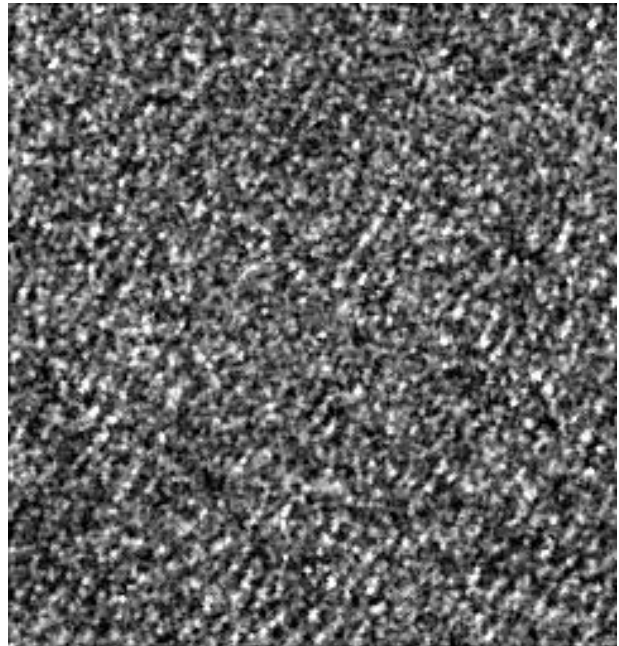
(d) Pre-processing II

(e) Intensity thresholding I
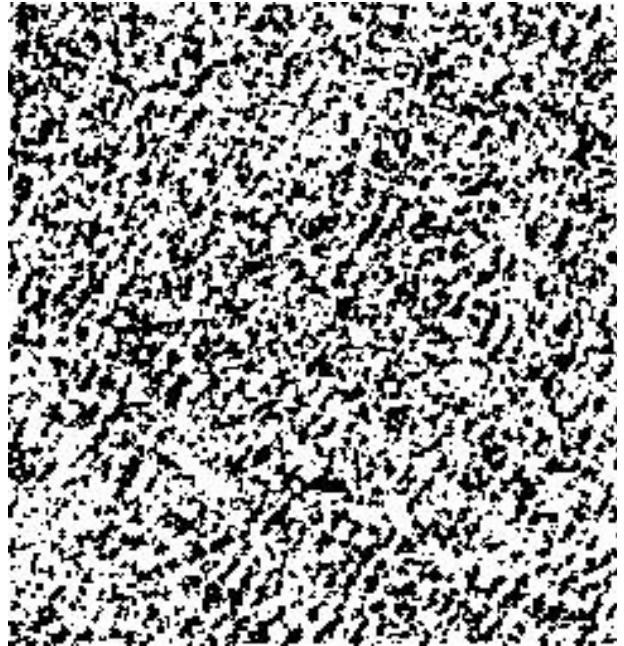
(f) Intensity thresholding II

(g) Normalized density estimation I
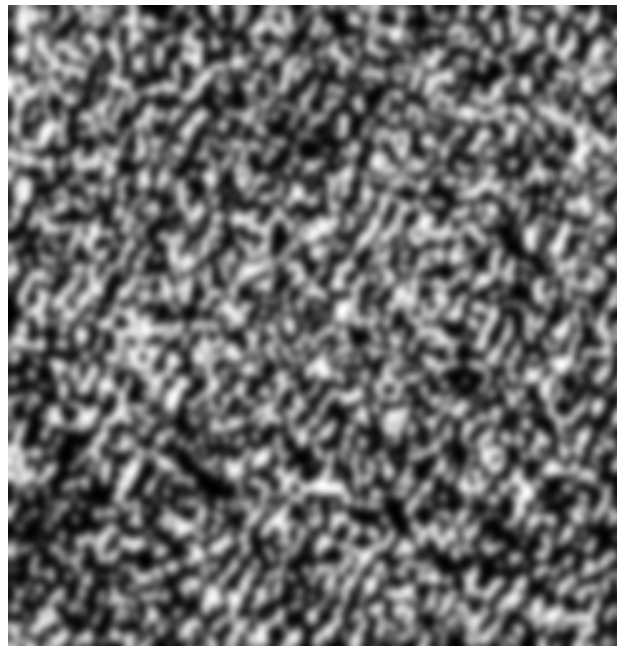

(h) Normalized density estimation II

(i) Spatial density thresholding I
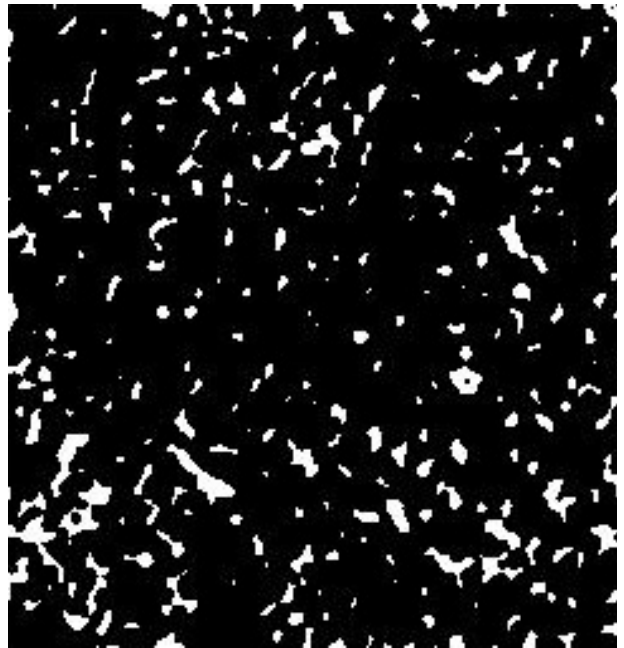
(j) Spatial density thresholding II

(k) Post-processing I
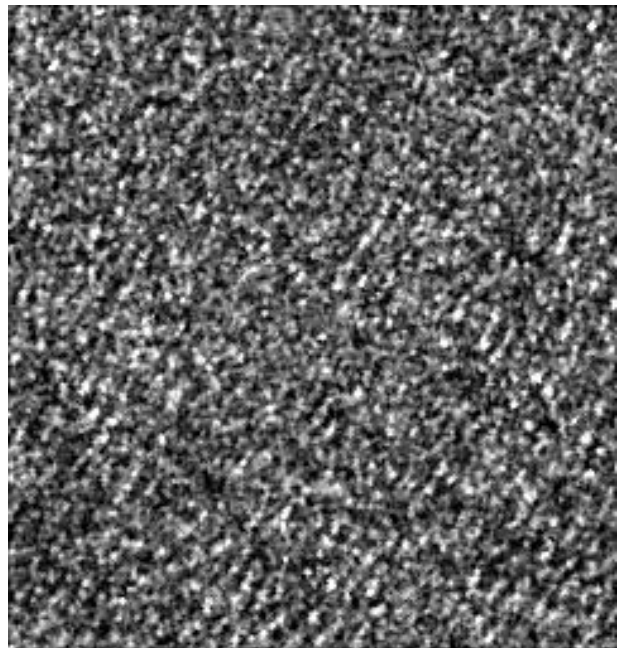
(l) Post-processing II

Figure 4.2. Illustration of results of the proposed approach at each step.

(a)   **(b)**
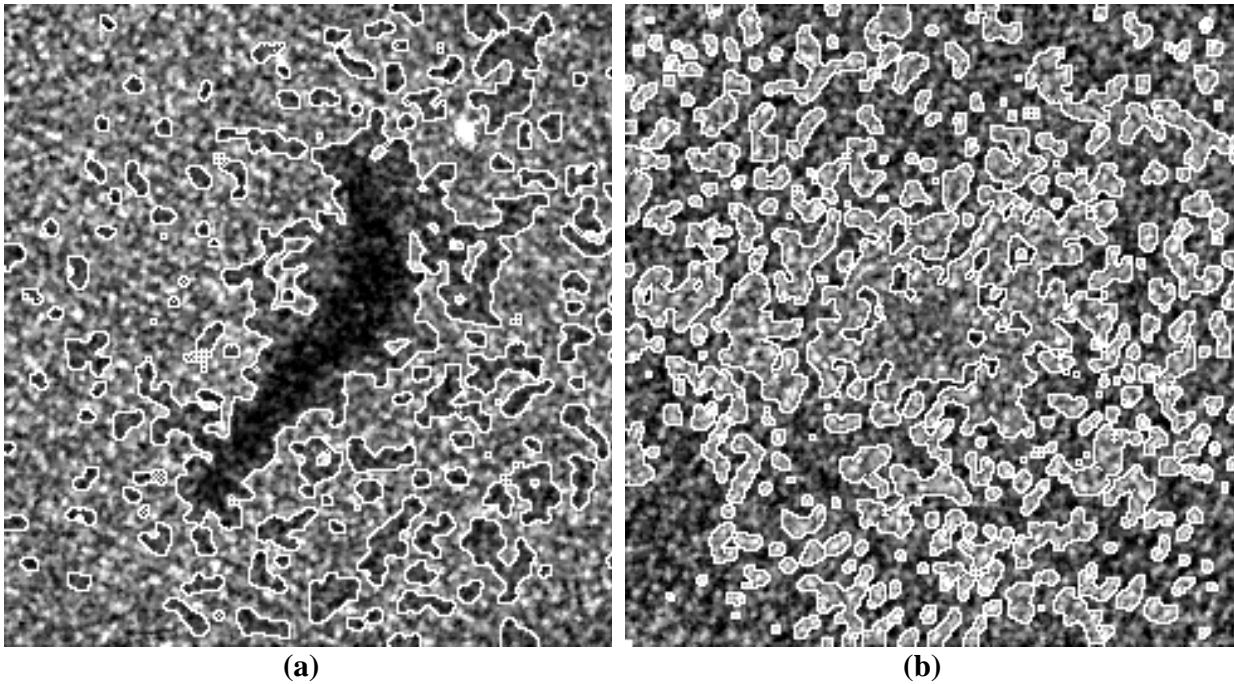
Figure 4.3. Illustration of detection results by the level set method.

To evaluate the detectability of the proposed approach on different types of anomalies, the whole evaluation dataset is divided into three groups: the well-defined versus the not-well-defined, the linear versus the massive, and the homogeneous background versus the heterogeneous background. The well-defined refers to those dark spots that have clear boundaries against the background and vice versa for the not-well-defined. Figure 4.4 illustrates results of the proposed method on some typical examples compared to that of level set segmentation method. The parameters for the level set method have been tuned for each image in order to achieve the optimal result in terms of visual inspection. In contrast, the proposed method use all the same parameter described in Section 4.2. The extracted boundaries (white lines) are overlaid on the contrast enhanced image for visual evaluation. Figure 4.4(a) shows a case of detection of a well-

defined massive dark spot in a homogeneous background. The size of the test image 1 is 256×256 pixels. Figure 4.4 (a1) shows the detection result by the level set method. Figure 4.4(a2) shows the detection result achieved by the proposed method. Figure 4.4(b) shows a case of detection of a not-well-defined massive dark spot in a homogeneous background. The size of evaluation image 2 is 256×256 pixels. Figure 4.4(b1) shows the detection result obtained by the level set method. Figure 4.4(b2) shows the detection result of the proposed method. Figure 4.4(c) shows the detection of a well-defined linear dark spot in a homogeneous background. The size of the test image 3 is 256×256 pixels. Figure 4.4(c1) shows the detection result of the level set method. Figure 4.4(c2) shows the detection result by the proposed method. Figure 4.4(d) shows the detection of a well-defined linear dark spot in a heterogeneous background. The size of the evaluation image 4 is 1024×1024 pixels. Figure 4.4(d1) shows the detection result by the level set method. Figure 4.4(d2) shows the detection result by the proposed method. Table 4.2 shows the quantitative comparison between the level set method and the proposed method on six evaluation images, including two evaluation images in Figure 4.3 and four test images in Figure 4.4. As shown in Table 4.2, the proposed method generates much less commission and omission error than the level set method on each of the six evaluation images. The computational time of the proposed method is also much shorter than that of the level set method for each evaluation image. Visual and quantitative comparison between the level set method and the proposed method all indicates that the latter achieve much better results than the former in various conditions, in terms of detection accuracy, algorithm robustness, and computational efficiency.

Table 4.3 reports the result of quantitative accuracy assessment result on the whole evaluation

dataset. The average commission error is 5.8% with the standard deviation of 0.11. 75%

detections have commission errors less than 5.8%. In the worst case, 56.7% commission error is

Table 4.2. Quantitative comparison between the level set method and the proposed method on six typical evaluation images.

|	Commission error		Omission error		Average error (pixel)		Computational time (second)	
	M1	M2	M1	M2	M1	M2	M1	M2
Figure 4.3 (a)	94.7%	3.2%	42.9%	0	0.1	0.2	258.6	1.8
Figure 4.3 (b)	100.0%	0	0	0	0	0	278.3	2.6
Figure 4.4 (a)	78.0%	0	3.4%	0	0.5	1.0	270.8	0.9
Figure 4.4 (b)	76.6%	0	6.7%	0	0.3	1.0	276.2	1.4
Figure 4.4 (c)	93.2%	0	10.8%	0	0.1	0.1	272.6	1.9
Figure 4.4 (d)	96.8%	53.2%	35.8%	4.2%	0.1	0.5	3431.7	17.2

M1: level set method; M2: the proposed method; The number of layer for buffer zone $n=4$.

produced by the proposed method. The average omission error is 4.6% with the standard

deviation of 0.14. 75% detections have omission errors less than 4.6%. For the worst case, 60.5%

omission error is made by the proposed method. The average error is 0.5 pixels with a standard

deviation of 0.45. The average number of false alarms is 1.1 per window. The average

computational time for one detecting window is 1.15 seconds. Table 4.4 demonstrates the

accuracy assessment on different types of anomalies. As shown in Table 4.4, the proposed method achieves better results on the well-defined dark spots than the not-well-defined ones. The commission error for the former is 3.7% versus 11.0% for the latter. And the omission error is 5.0% for the former compared to 11.0% for the latter. Also, the method generates more omission error and less commission error on linear dark spots than the massive ones. The omission and commission error for the linear are 10.8% and 4.1% compared to 3.5% and 7.1% for the massive, respectively. Furthermore, the method produces much worse results in a heterogeneous background than in a homogeneous background. 19.7% of commission error and 22.9% of omission error are generated in the case of heterogeneous background. In contrast, only 4.2% commission error and 4.8% omission error are produced in the homogeneous background.


**(a) Evaluation image 1 (E1)**　　　　　　**(b) Evaluation image 2 (E2)**
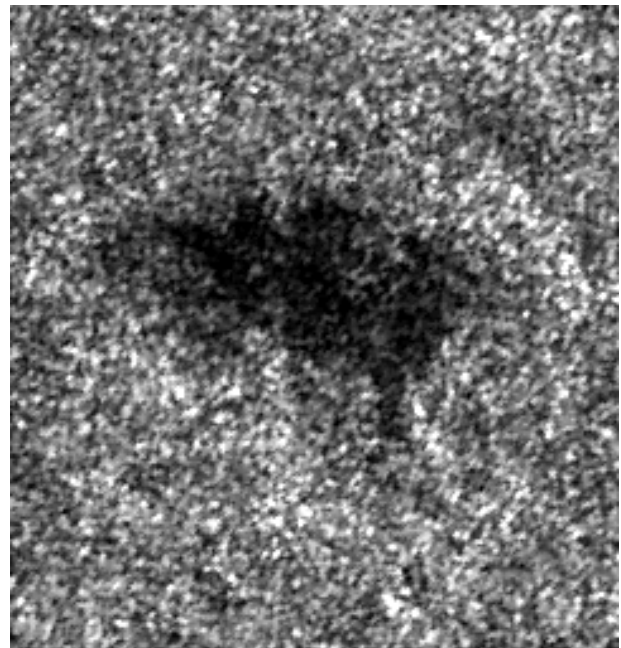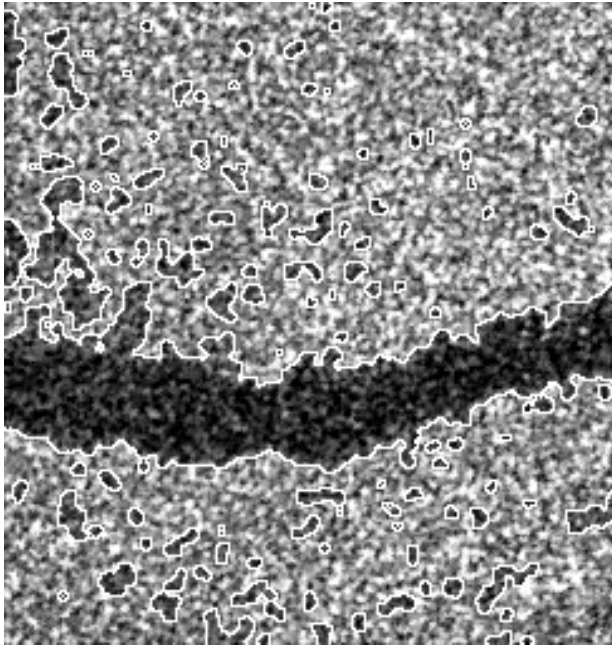
(a1) Result of E1 by the level set
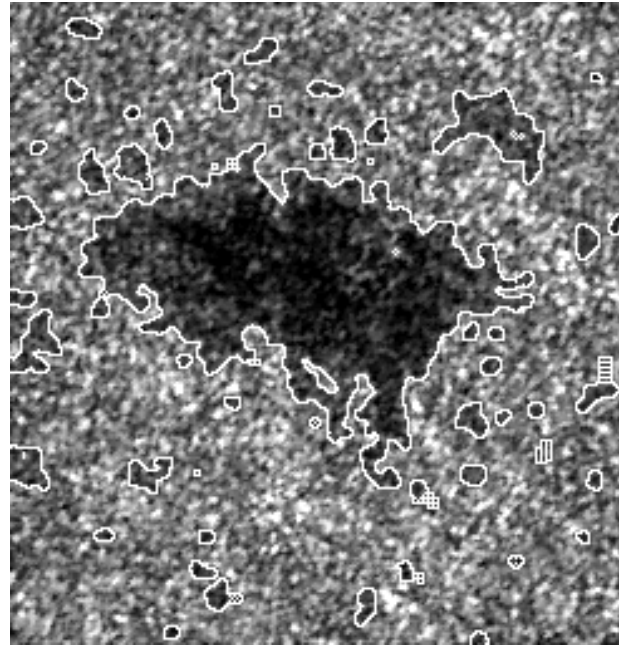
**(b1) Result of E2 by the level set**
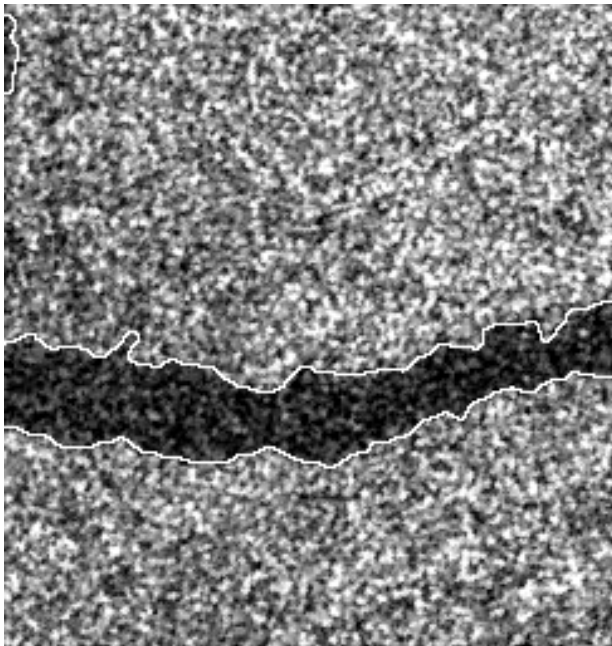

(a2) Result of E1 by the proposed method
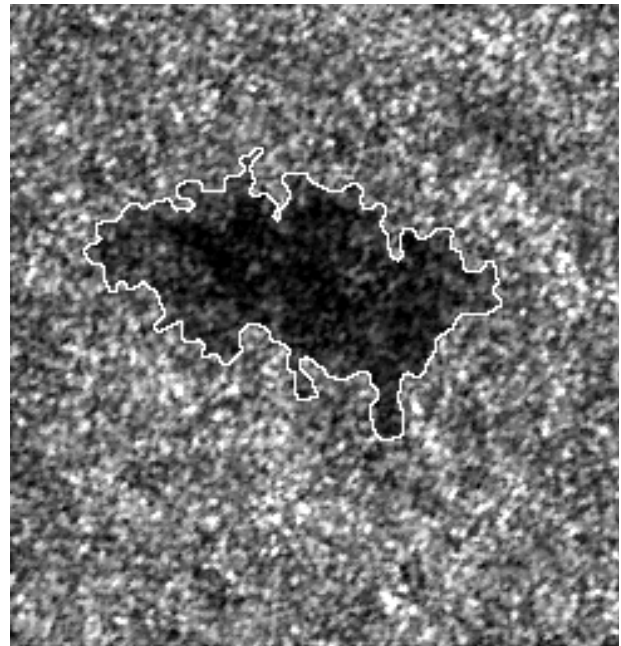
**(b2) Result of E2 by the proposed method**
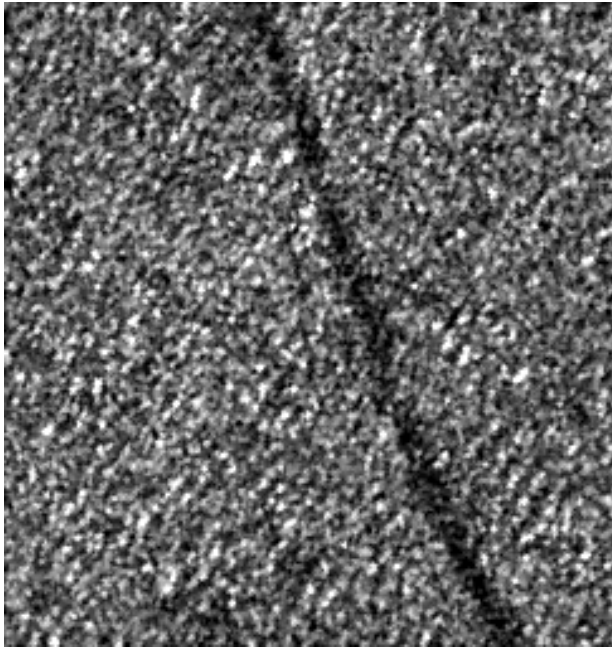
(c) Evaluation image 3 (E3)
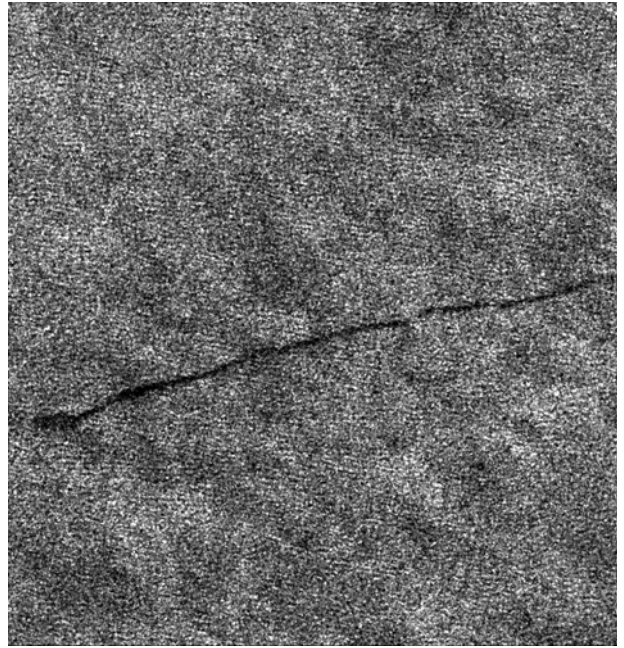
(d) Evaluation image 4 (E4)
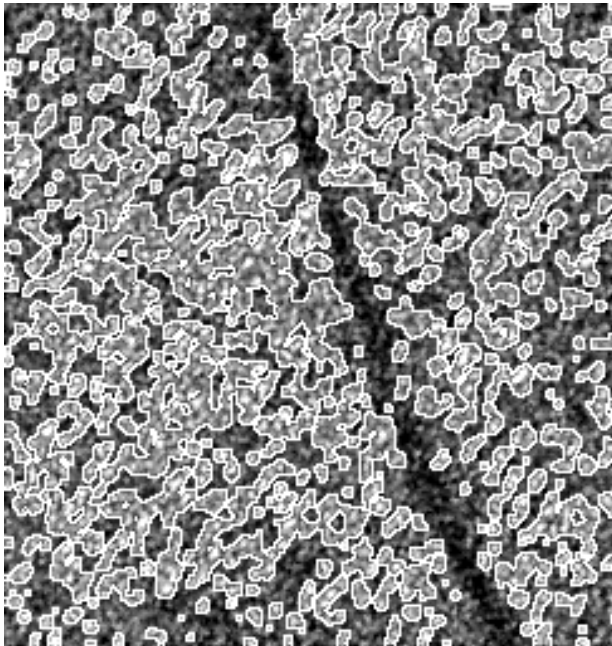
(c1) Result of E3 by the level set
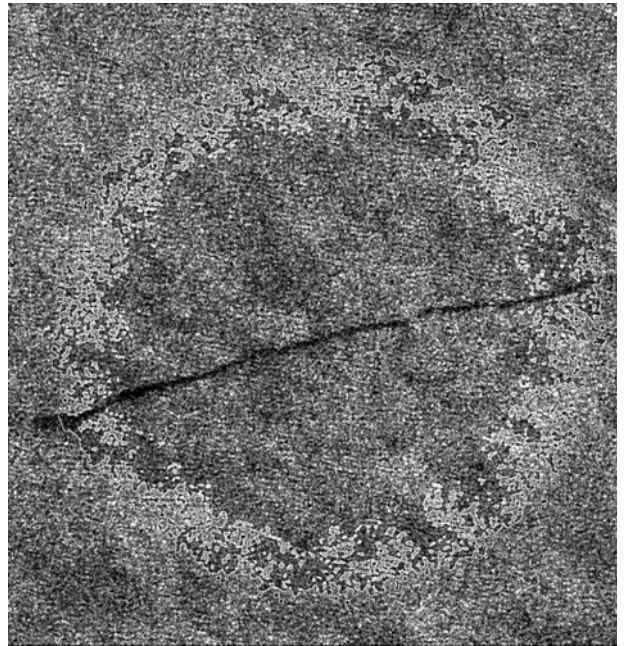
(d1) Result of E4 by the level set

67
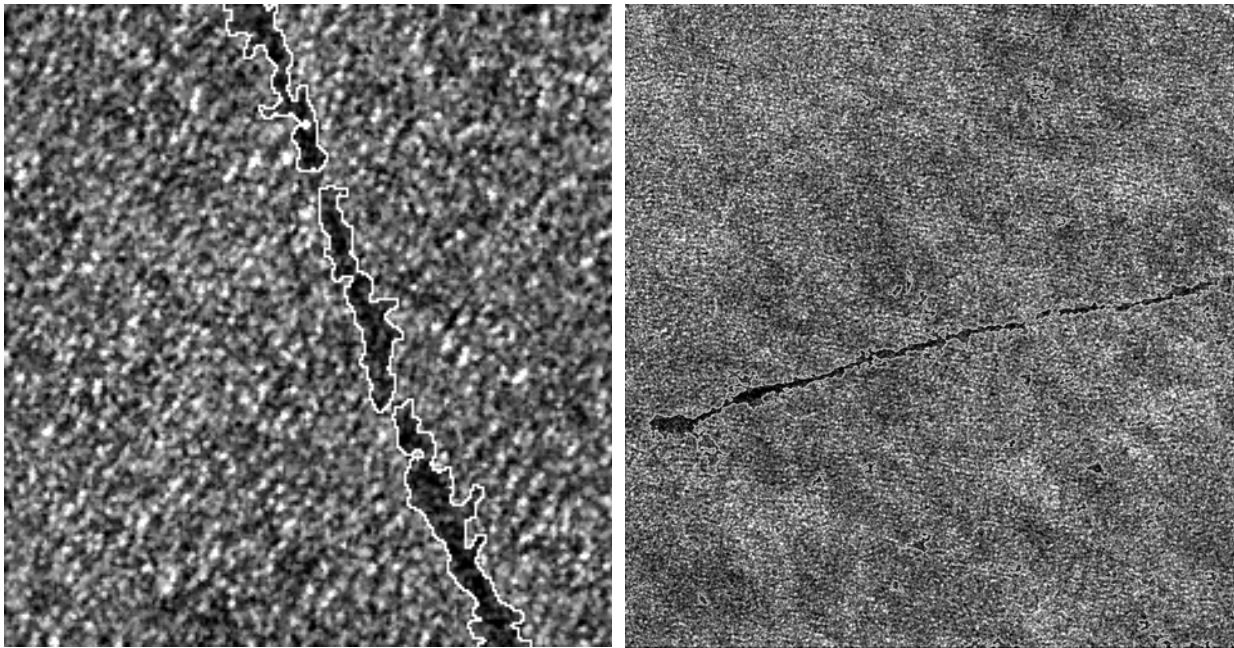
(c2) Result of E3 by the proposed method   **(d2) Result of E4 by the proposed method**

Figure 4.4. Visual comparison of detecting different types of dark spots between the level set method and the proposed method.

Table 4.3. Accuracy assessment on the whole evaluation dataset.

	Min	Max	Mean	75% Percentile	Standard deviation
Commission error	0.0%	56.7 %	5.8%	5.8%	0.11
Omission error	0.0%	60.5%	6.6%	4.6%	0.14
Average error	0.0	1.1	0.5	1.01	0.45

The size of buffer zone $n=4$.

**Table 4.4. Accuracy assessment on different types of anomalies.**

|	Commission error	Omission error	Average error	Number of the cases
Well-defined	3.7%	5.0%	0.5	43

Not-well-defined	11.0%	11.0%	0.5	17
Linear	4.1%	10.8%	0.5	25
Massive	7.1%	3.5%	0.5	35
Homogeneous	4.2%	4.8%	0.5	54
Heterogeneous	19.7%	22.9%	0.3	6

The size of buffer zone $n=4$.

It is necessary to further pick out those "worse results" and see why the proposed method failed to work properly in those cases. Figure 4.5 illustrates two typical examples. The left-hand side shows the original images after pre-processing and the right-hand side shows the detection results. In Figure 4.5(a), the proposed method failed because the dark slick is too thin and its contrast in some of part is also too low. Human operators manage to delineate the border in Figure 4.5(a) because of incorporating their knowledge on linear feature. In Figure 4.5(b), the proposed method failed because the background is very heterogeneous. As seen from the image, there are two types of dominate intensities in the background, which made the adaptive intensity threshold failed to work properly. After the intensity threshold segmentation, both the dark spot and the background have areas where the density of dark pixels is low. Therefore, it is difficult for the proposed approach to well discriminate between the dark spot and the background.
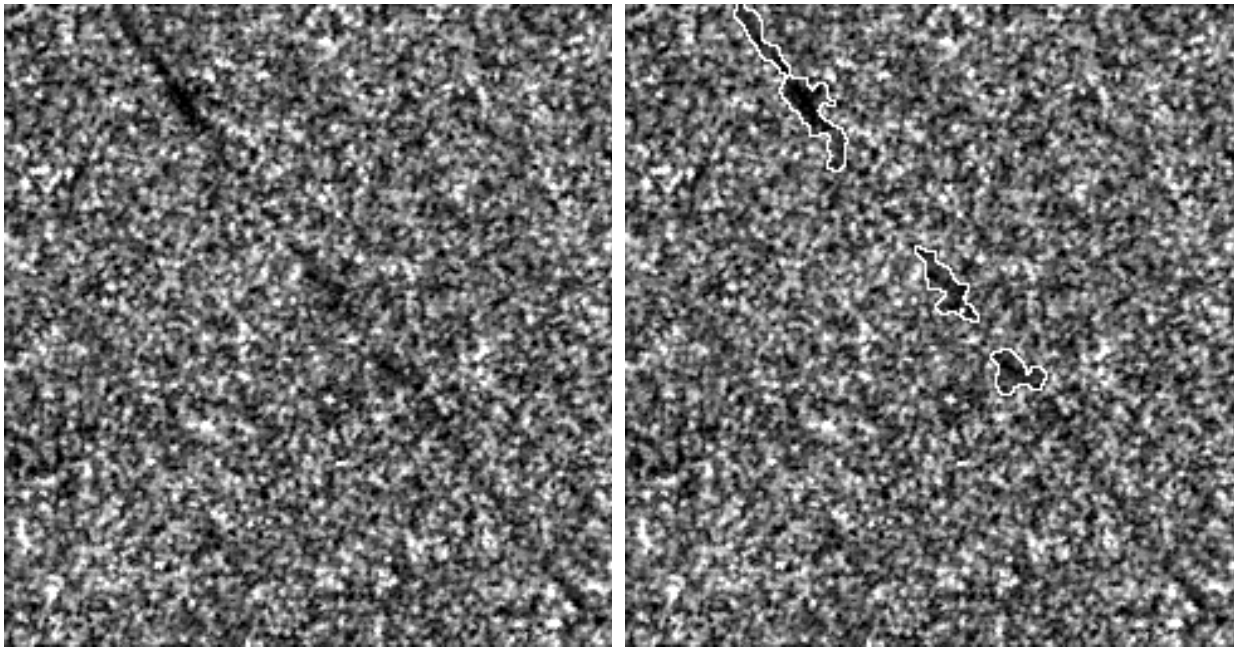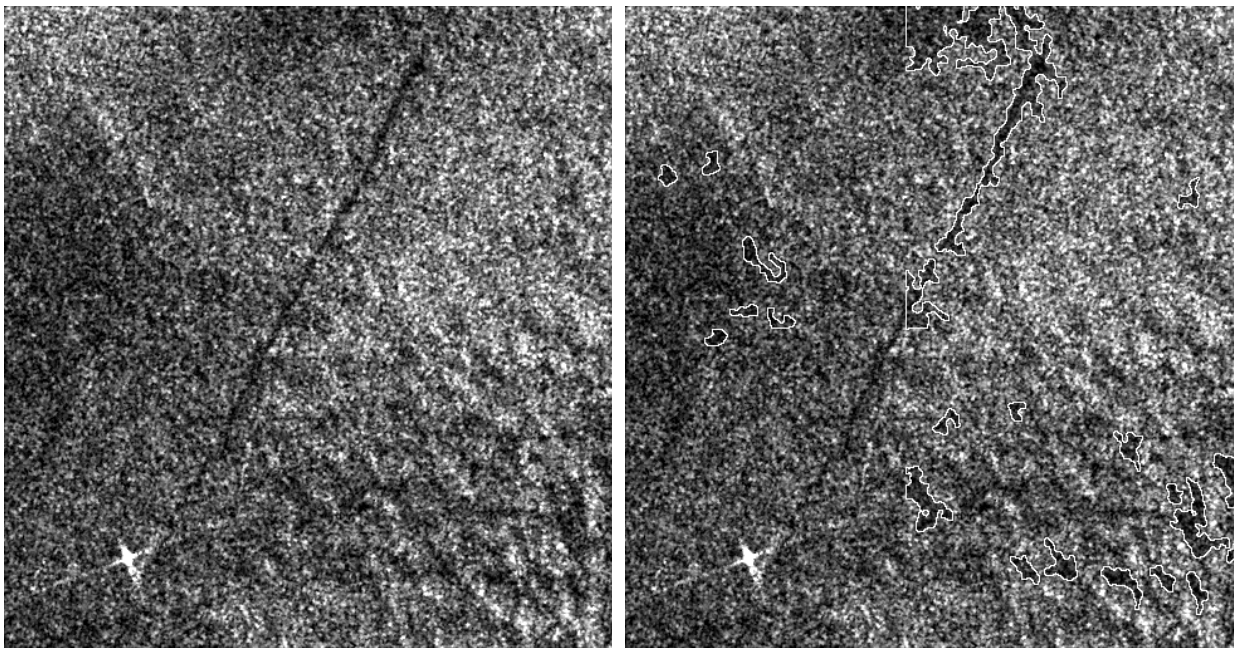
Figure 4.5. Two examples on which the proposed method works quite improperly.

4.4 Chapter Summary

In this chapter, the results of dark spot detection by the proposed method on different evaluation SAR intensity images have been presented. The automatically detected results are qualitatively evaluated in comparison to the results by level set segmentation method on some typical images. It is also quantitatively evaluated with respect to manual detection. The performance of the proposed method is satisfactory based on the evaluation analysis.

Chapter 5

Conclusions and Recommendations for Future Work

This chapter summarizes conclusions of this thesis. Recommendations for further research are also given.

5.1 Conclusions

This thesis deals with the task of developing an automated method for dark spot detection from SAR intensity imagery for marine oil spill monitoring. A novel method called spatial density thresholding is proposed for the purpose. This method achieved promising results in terms of detection accuracy, algorithm robustness, and computational efficiency.

Two main difficulties lie in the detection of dark spots from SAR intensity imagery. One is the speckle noises. The other one is the various contrasts between dark spots and the background. To overcome these difficulties, apart from using the common intensity feature, the method utilizes the spatial density feature to further discriminate between dark spots and background. It was motivated by the facts that speckles noises are randomly distributed in the spatial domain. Theoretic reasoning on why utilizing the spatial density feature can increase the detection probability of a dark spot increases while reducing the probability of a false alarm is addressed based on Bayesian inference and principles of SAR imaging.

The method consists of two main steps. In the first step, pixels are partitioned into two classes according to their intensity distributions. Otsu's adaptive intensity thresholding method is utilized, which aims to find the optimal threshold that maximizes the ratio of between-class variance to the within-class variance. Pixels with intensity below the threshold are regarded potential dark spots and the others are regarded as potential background. In the second step, the spatial density of potential background is estimated. Pixels are partitioned further according to their spatial density distributions. A spatial density threshold is selected. Pixels with density below the threshold are the real dark spot pixels, while the others with density above the threshold are the real background pixels.

To verify the effectiveness of the proposed method, it was tuned and applied to an evaluation dataset containing 60 RADARSAT-1 ScanSAR Narrow Beam intensity images which cover all available anomaly cases from the ISTOP oil spill target database detected between 2006 and 2008. The same parameters were used for all the evaluation images. To study the performance of the proposed method on different types of oil spills, the evaluation dataset was divided into three groups, the well-defined versus the not-well-defined, the linear versus the massive, and the homogeneous background versus the heterogeneous background. A comparison between the proposed method and the Chan-Vese level set method on some typical images indicates the proposed method achieved much better results than the level set method in terms of detection accuracy, algorithm robustness and computational efficiency. To quantitatively assess the accuracy of detection results, a reference dataset was produced by manual interpretation and the buffer zone approach was utilized. The proposed method achieved an average of 5.8%

commission, 6.8% omission and 0.5 pixels error for the overall evaluation dataset, respectively. The average number of false alarms is 1.1 per detecting window and the average computational time per window is 1.15 seconds, respectively, on the PC-based MATLAB 7.0 platform. Evaluation results shows that the proposed method works better in case of the well-defined, the massive and the homogeneous background as opposed to the cases of the not-well-defined, the linear, and the heterogeneous background, respectively.

In summary, the contributions of this thesis include: 1) releasing the speckle noises and various degree of contrasts between darks spots and background are the two main difficulties for automated dark spot detection from SAR intensity imagery, 2) driving the attention from intensity domain to spatial domain and developing an novel spatial density thresholding for automated dark spot detection from SAR intensity imagery, and 3) investigating the performance of spatial density thresholding on dark spot detection from SAR intensity imagery under various conditions and demonstrating the method is effective, fast and reliable, and is very promising for fully-automated marine oil spill detection in practice.

5.2 Recommendations for Future Research

5.2.1 Use of Anisotropic Kernel

As illustrated in the experiment, the proposed method works improperly in detecting some linear dark spots. To overcome the problem, prior information on linear feature should be incorporated into the detection. Instead of using the symmetric Gaussian kernel, the anisotropic kernel which

favors linear feature can be applied to estimate local density. Jue et al. (2004) proposed an anisotropic kernel mean shift for image and video segmentation, which achieved much better results in the linear feature segmentation than the original mean shift algorithm developed by Comaniciu & Meer (2002). Similar anisotropic kernel can be utilized here to improve the detection of linear dark spots. Botev's diffusion model for nonparametric density estimation used in the thesis is easy to incorporate such prior information. A more generalized diffusion model to integrate prior information has been elaborated in Botev (2009), which is given by

$$\frac{\partial}{\partial t} g(x;t) = L[g(x)], \qquad x \in R, t > 0, \tag{5.1}$$

where the linear differential operator $L[\cdot] = \frac{1}{2}\frac{d}{dx}(a(x)\frac{d}{dx}(\frac{\cdot}{p(x)}))$, $a(x)$ is an arbitrary positive function on R and the initial condition is $g(x,0) = \Delta(x)$. The $p(x)$ is the prior information. By using incorporating the anisotropic kernel as the prior information into the diffusion model, the detectability of dark spots with linear feature would expect to be enhanced.

5.2.2 Application of Multi-scale Technique

Heterogeneous background is another problem that needs to be addressed in the future. One possible solution is to utilize the multi-scale techniques. The basic idea is to decompose a heterogeneous background into several small homogeneous regions where the proposed method is able to work appropriately. The multi-scale detecting windows can be employed for this

purpose. Instead of using the fixed size window as proposed in this thesis, a detecting pyramid can be created with windows from the small to the large. The dark spot detected at the different scales are to combine to form the final result. However, other issues needs to be further addressed may include how to design a proper detecting pyramid and how to combine the detection results obtained at different scales.

5.2.3 Implementation of Parallel Computing

As can be seen from the implementation of the proposed method, detection processes in individual windows are independent from one to another. In other words, no data exchanging occurs among individual windows during the detection processes. Therefore, the proposed method can be further implemented in a parallel computing. According to the number of computing nodes (computers taking charge of the computing) available in a parallel system, the input SAR data can be divided equally and transmitted to each computing node for the dark spot detection by the management node (computer taking charge of the entire operation). Dark spots detected at individual computing nodes are then to transmit back to the management node where they are mosaicked to form the final result. The implementation of parallel computing would realize the real-time dark spot detection for marine oil spill monitoring.

5.2.4 Investigation on Potential of RADARSAT-2 for Oil Spill Monitoring

Canadian Space Agency (CSA)'s RADARSAT program is to strategically improve Canada's marine monitoring capability. Newly launched RADARSAT-2 provides all imaging modes of

RADARSAT-1 as well as some new modes that incorporate significant innovations and improvements (van der Sanden, 2004). For example, RADARSAT-2 provides ultra-fine beam mode with 3m spatial resolution and operates in three polarization modes: the selective single polarization with a single channel (HH or HV or VH or VV), the selective dual polarization (dual-pol) with a like- and cross-polarized radar channel (HH and HV or VV and VH), and the quad polarimetric (quad-pol) mode with four available transmit and receive linear antenna polarization combinations (HH, HV, VV, VH), also called fully polarimetric mode. The potential of new imaging modes of RADARSAT-2 for oil spill monitoring will be investigated in the future.

References

Adalsteninsson, D., & Sethiant, J. A. (1995). A fast level set method for propagating interfaces. *Journal of Computational Physics, vol. 118,* 269-277.

Alpers, W., & Huehnerfuss, H. (1988). Radar signature of oil film floating on the sea surface and the Marangoni effect. *Journal of Geophysical Research, vol. 93(C4),* 3642-3648.

Alpers, W., & Huehnerfuss, H. (1989). The damping of ocean waves by surface films—a new look at an old problem. *Journal of Geophysical Research—Oceans, vol. 94(C4): 6251-6265.*

Alpers, W., Wismann, V., Theis, R., Huhnerfuss, H., Bartsch, N., Moreira, J., & Lyden, J. (1991). The damping of ocean surface waves by monomolecular sea slicks measured by airborne multifrequency radars during the saxon-fpn experiment. *Proceedings of IEEE International Geoscience and Remote Sensing Symposium (IGARSS'91), Helsinki, Finland,* 1987-1990.

Bishop, C. M. (2006). *Pattern Recognition and Machine Learning.* Springer.

Brekke, C., & Solberg, A. H. S. (2005). Oil spill detection by satellite remote sensing. *Remote Sensing of Environment, vol. 95(1)*, 1-13.

Botev, Z. I. (2009). Kernel density estimation via diffusion mixing. [Online]. Available: http://www.maths.uq.edu.au/~botev/

CCRS. (2009). *Fundamentals of Remote Sensing.* Canada Centre for Remote Sensing. [Online]. Available: http://ccrs.nrcan.gc.ca/resource/index_e.php#tutor.

Chan, T. F., & Vese, L. A., (2001). Active contours without edges. *IEEE Transactions on Image Processing, vol. 10(2),* 266-277.

Chang, L., Tang, Z. S., Chang, S. H., &, Chang Y. L. (2008). A region-based GLRT detection of oil spills in SAR images*. Pattern Recognition Letters, vol. 29,* 1915-1923.

Chaudhuri, P., & Marron, J. S. (2000). Scale space view of curve estimation. *The Annals of Statistics, vol. 28(2),* 408-428.

Chen, C. F., Chen, K. S., Chang, L. Y., & Chen, A. J. (1997). The use of satellite imagery for monitoring coastal environment in Taiwan. *Proceedings of IEEE International Geoscience and Remote Sensing Symposium (IGARSS'97), vol. 3,* 1424-1426.

Clemente-Colon, P. & Yan, X. H. (2000). Low backscatter ocean features in Synthetic Aperture Radar imagery. *John Hopkins APL Technical Digest*, *vol. 21(1),* 116-121.

Comaniciu, D., & Meer, P. (2002). Mean shift: a robust approach toward feature space analysis. *IEEE Transactions on Pattern Analysis and Machine Intelligence, vol. 24(5),* 1-18.

Derrode, S., & Mercier, G. (2006). Unsupervised multiscale oil slick segmentation from SAR images using a vector HMC model. *Pattern Recognition, vol. 40(3),* 1135-1147.

Definiens. (2000). eCognition User Guide. [Online]. Available: http://www.gis.unbc.ca/help/software/ecognition4/ELuserguide.pdf

Elachi, C. (1980). Spaceborne imaging radar: geologic and oceanographic applications. *Science, vol. 4461,* 1073-1082.

Espedal, H. A., & Wahl, T. (1999). Satellite SAR oil spill detection using wind history information. *International Journal of Remote Sensing. vol. 20(1),* 49-65.

Espedal, H. A., & Johannessen, O. M. (2000). Detection of oil spills near offshore installations using synthetic aperture radar (SAR). *International Journal of Remote Sensing, vol. 21(11),* 2141-2144.

Evans, D. L., Alpers, W., Cazenavec, A., Elachia, C., Farra, T., Glackind, D., Holta, B., Jonese, L., Liua, W. T., McCandlessf, W., Menardg, Y., Mooreh, R., & Njokua, E. (2005). Seasat—A 25-year legacy of success. *Remote Sensing of Environment, vol. 94,* 384-404.

European Space Agency. (1998). Oil pollution monitoring. *ESA Brochure: ERS and Its Application—Marine, BR-128,* 1.

Fortuny-Guasch, J. (2003). Improved Oil Slick Detection and Classification with Polarimetric SAR. *Proceedings of Workshop on Application of SAR Polarimetry and Polarimetric Interferometry, ESA-ESRIN Frascati, Italy.*

Frate, F. D., Petrocchi, A., Lichtenegger, J., & Calabresi, G. (2000). Neural networks for oil spill detection using ERS-SAR data. *IEEE Transactions on Geoscience and Remote Sensing, vol. 38(5),* 2282-2287.

Fukunaga,K. (1990). *Introduction to Statistical Pattern Recognition,* 2nd edition. San Diego, CA: Academic Press Professional.

Gade, M. & Alpers, W. (1999). Using ERS-2 SAR images for routine observation of marine oil pollution in European coastal waters. *The Science of The Total Environment, vol. 273-238,* 441-448.

Gade, M., Alpers, W., & Bao, M. (1996). Measurements of the radar backscattering over different oceanic surface films during the SIR-C/X-SAR campaigns. *Proceedings of International Geoscience and Remote Sensing Symposium (IGARSS'96),* 860-862.

Gade, M., Alpers, W., Hühnerfuss, H., Masuko, H., & Kobayashi, T. (1998). Imaging of biogenic and anthropogenic ocean surface films by the multifrequency / multipolarization SIR-C / X-SAR. *Journal of Geophysical Research, vol. 103(C9),* 18851-18866.

Gambardella, A., Migliaccio, M. & De Grandi, G. (2007). Wavelet polarimetric SAR signature analysis of sea oil spills and look-alike features. *Proceedings of IEEE International Geoscience and Remote Sensing Symposium (IGARSS'07), Barcelona, Spain,* 983-986.

Gauthier, M. F., Weir, L., Ou, Z., Arkett, M., & De Abreu, R. (2007). Integrated satellite tracking of pollution: a new operational program, *Proceedings of IEEE International Geoscience and Remote Sensing Symposium (IGARSS'07), Barcelona, Spain,* 967-970.

Gens, R. (2008). Oceanographic application of SAR remote sensing. *GIScience & Remote Sensing, vol. 45(3),* 275-305.

Gin, K. Y. H., Huda, MD. K., Lim, W. K., & Tkalich, P. (2001). An oil spill-food chain interaction model for coastal waters. *Marine Pollution Bulletin, vol. 42(7),* 590-597.

Girard-Ardhuin, F., Mercier, G., Collard, F. & Garello, R. (2005). Operational Oil-Slick Characterization by SAR Imagery and Synergistic Data. *IEEE Transactions on Geoscience and Remote Sensing, vol. 3,* 487-495.

Gonzalez, R. C., & Woods, R. E. (2002). *Digital Image Processing, 2nd edition.* New Jersey: Prentice-Hall.

Henschel, M. D., Olsen, R. B., Hoyt, P., & Vachon, P. W. (1997). The ocean monitoring workstation experience gained with Radarsat, *Geomatics in the Ear of Radarsat (GER'97), Ottawa, ON.*

Hofer, T. (2003). Tanker safety and coastal environmental: Prestige, Erika, and what else? *Environmental Science and Pollution Research, vol. 10(1),* 1-5.

Hovland, H.A., Johannessen, J.A., & Digranes, G. (1994). Slick detection in SAR images. *Proceedings of IEEE International Geoscience and Remote Sensing Symposium (IGARSS 94), Pasadena, CA, vol. 4,* 2038-2040.

Huang, B., Li, H., & Huang, X. (2005). A level set method for oil slick segmentation in SAR images. *International Journal of Remote Sensing, vol. 26(6),* 1145-1156.

Jha, M. N., Levy, J., & Gao, Y. (2008). Advances in remote sensing for oil spill disaster management: state-of-the-art sensors technology for oil spill surveillance. *Sensors, vol. 8,* 236-255.

Jones, M., Marron, J., & Sheather, S. (1996). A brief survey of bandwidth selection for density estimation. *Journal of the American Statistical Association, vol. 91*, 401-407.

Kass, M., Witkin, A., & Terzopoulos, D. (1987). Snakes: Active contour models. *International Journal of Computer Vision*, 321-331.

Karathanassi, V., Topouzelis, K., Pavlakis, P., & Rokos, D. (2006). An object-oriented methodology to detect oil spills. *International Journal of Remote Sensing, vol. 27,* 5235-5251.

Karantzalos, K., & Argialas, D. (2008). Automatic detection and tracking of oil spills in SAR imagery with level set segmentation. . *International Journal of Remote Sensing, vol. 29(21),* 6281-6296.

Li, Y., Li, J., & Lu, Y. (2008). A fuzzy segmentation-based approach to extraction of coastlines from IKONOS imagery. *Geomatica*, *vol. 62 (4),* 407-417.

Li, Y, & Li, J. (2010). Oil spill detection from SAR intensity image using marked point process. *Remote Sensing of Environment, accepted subject to revision.*

Lindeberg, T. (1994). *Scale Space Theory in Computer Vision.* Boston: Kluwer.

Liu, A. K., Peng, C. Y., & Chang, S. Y. (1997). Wavelet analysis of satellite images for costal watch. *IEEE Journal of Ocean Engineering, vol. 22,* 9-17.

Maio, A. D., Ricci, G., & Tesauro, M. (2001). On CFAR detection of oil slicks on the ocean surface by multifrequency and/or multipolarization SAR. *Proceedings of 2001 IEEE Radar Conference,* 351-356.

Malinovsky, V. V., Sandven, S., Mironov, A. S. & Korinenko, A. E. (2007). Identification of oil spills based on ratio of alternating polarization images from ENVISAT. *Proceedings of IEEE International Geoscience and Remote Sensing Symposium (IGARSS' 07), Barcelona, Spain,* 1326-1329.

Martin, S. (2004). *An Introduction to Ocean Remote Sensing*. London: Cambridge University Press.

Masuko, H., Kobayashi, T., Okamoto, K., & Alpers, W. (1995). Observation of artificial slicks with SIR-C/X-SAR around Japan. *Proceedings of IEEE International Geoscience and Remote Sensing Symposium (IGARSS' 95), Florence, Italy, vol. 1,* 227-229.

Mercier, G., & Girard-Ardhuin, F. (2006). Partially supervised oil-slick detection by SAR Imagery using kernel expansion. *IEEE Transactions on Geoscience and Remote Sensing, 44(10),* 2839-2846.

Migliaccio, M., Gambardella A., & Tranfaglia, M. (2007). SAR Polarimetry to Observe Oil Spills. *IEEE Transactions on Geoscience and Remote Sensing, vol. 2,* 506-511.

Munson, Jr. D. C. & Visentin, R. L. (1989). A signal processing view of strip-mapping synthetic aperture radar. *IEEE Transactions on Acoustics, Speech and Signal Processing*, *vol. 37(12),* 2131-2147.

Neville, R. A., Thomson, V., Gray, A. L., & Hawkins, R. K. (1984). Observation of two test oil spills with a microwave scatterometer and a synthetic aperture radar. *Remote Sensing for the Control of Marine Pollution,* 257-266.

Nirchio, F., Sorgente, M., Giancaspro, A., Biamino, W., Parisato, E., Ravera, R., & Tribero, P. (2005). Automatic detection of oil spills from SAR images. *International Journal of Remote Sensing, vol. 26(6),* 1157-1174.

NOAA. (1992). Oil Spill Case Histories 1967 – 1991, *Report No. HMRAD 92-11, Seattle, 80p.*

Novak, L. M., Owirka, G. J., & Netishen, C. M. (1993). Performance of a high-resolution polarimetric SAR automatic target recognition. *Lincoln Laboratory Journal.*

Oliver, C., & Quegan, S. (1998). *Understanding Synthetic Aperture Radar Images.* London: Artech House.

Osher, S., & Sethian, J. A. (1988). Fronts propagating with curvature-dependent speed: algorithms based on Hamilton-Jacobi formulations. *Journal of Computational Physics, vol. 79,* 12-49.

Otsu, N. (1975). A threshold selection method from gray-level histograms. *IEEE Transactions on Systems, Man, and Cybernetics, vol. 9(1),* 62-65.

Pavlakis, P., Sieber, A., & Alexandry, S. (1996). Monitoring oil-spill pollution in the Mediterranean with ERS SAR. *ESA Earth Observation Quarterly vol. 52,* 8-11.

Richards, J. A. and Jia, X. 2006. Remote Sensing Digital Image Analysis, 4th ed.; Berlin, Germany: Springer-Verlag, 67-238.

Shapiro, L. G., & Stockman, G. C. (2001). *Computer Vision.* New Jersey: Prentice-Hall.

Singh, K. P., Gray, A. L., Hawkins, R. K., & O'Neil, R. A. (1986). The influence of surface oil on C- and Ku-band ocean backscatter. *IEEE Transactions on Geoscience and Remote Sensing, vol. GE-24 (5),* 738-744.

Soille, P. (1999). *Morphological Image Analysis: Principles and Applications.* Springer-Verlag.

Solberg, A. H. S., Brekke, C., & Husøy, P. O. (2007). Oil spill detection in Radarsat and Envisat SAR Images. *IEEE Transactions on Geoscience and Remote Sensing, vol. 45(3),* 746-755.

Solberg, A. H. S., Storvik, G., Solberg, R., & Volden, E. (1999). Automatic detection of oil spills in ERS SAR images. *IEEE Transactions on Geoscience and Remote Sensing, vol. 37(4),* 1916-1924.

Solberg, A. H. S., & Volden, E. (1997). Incorporation of prior knowledge in automatic classification of oil spills in ERS SAR images. *Proceedings of IEEE International Geoscience and Remote Sensing Symposium (IGARSS'97), vol. 1,* 157-159.

Tseng, F. S. (1999). Consideration in care for birds affected by oil spills. *Seminars in Avian and Exotic Pet Medicine, vol. 8(1),* 21-31.

Topouzelis, K. N. (2008). Oil spill detection by SAR images: dark formation detection, feature extraction and classification. *Sensors, vol. 8,* 6642-6659.

Topouzelis, K. N., Karathanassi, V., Pavlakis, P., & Rokos, D. (2008). Dark formation detection using neural networks. *ISPRS Journal of Photogrammetry and Remote Sensing, vol. 29,* 4705-4720.

Ulaby, F. T., Moore, R. K. & Fung, A. K. (1982). *Microwave Remote Sensing: Active and Passive.* Addison-Wesley, MA.

van der Sanden, J. J. (2004). Anticipated applications potential of RADARSAT-2 data, *Canadian Journal of Remote Sensing, vol. 30(3),* 369-379.

Wang, J., Thiesson, B., Xu, Y., & Cohen, M. (2004). Image and video segmentation by anisotropic kernel mean shift. *Lecture Notes in Computer Science, vol. 3022,* 238-249.

Wismann, V., Gade, M., Alpers, W., & Hühnerfuss, H. (1998). Radar signatures of marine mineral oil spills measured by an airborne multi-frequency radar. *International Journal of Remote Sensing, vol. 19(18),* 3607-3623.

Yu, Y., & Acton, S. T. (2002). Speckle reducing anisotropic diffusion. *IEEE Transactions on Image Processing, vol. 11(11),* 1260-1270.